International Journal of Mechanical Sciences 242 (2023) 107967

Contents lists available at ScienceDirect

International Journal of Mechanical Sciences

journal homepage: www.elsevier.com/locate/ijmecsci

A method to measure non-Newtonian fluids viscosity using inertial viscometer with a computer vision system

Elena P. Kornaeva [a,*], Ivan N. Stebakov [b], Alexey V. Kornaev [b,c], Viktor V. Dremin [d,e], Sergey G. Popov [b], Andrey Yu. Vinokurov [f]

[a] Department of Information Systems and Digital Technologies, Orel State University, 95 Komsomolskaya St., Orel, 302026, Russia
[b] Department of Mechatronics, Mechanics, and Robotics, Orel State University, 95 Komsomolskaya St., Orel, 302026, Russia
[c] Research Center for Artificial Intelligence, Innopolis University, 1 Universitetskaya St., Innopolis, 420500, Russia
[d] Research and Development Center of Biomedical Photonics, Orel State University, 95 Komsomolskaya St., Orel, 302026, Russia
[e] College of Engineering and Physical Sciences, Aston University, Aston St., Birmingham, B4 7ET, UK
[f] Department of Industrial Chemistry and Biotechnology, Orel State University, 95 Komsomolskaya St., Orel, 302026, Russia

ARTICLE INFO

Keywords:
Non-Newtonian fluid
Viscosity
Inertial viscometer
Laser speckle-contrast imaging
Navier–Stokes equations
Deep learning

ABSTRACT

The theory of rheology of non-Newtonian fluids is based on the generalized Newtonian hypothesis of viscosity. The viscometers for non-Newtonian fluids should implement fluid flows with the known stress and strain state parameters distributions. Ideally, the distributions should be homogeneous in the flow domain. The idea of the proposed method is based on a combination of a capillary and a rotational viscometers implemented in the torus-shaped capillary viscometer. Analysis of the mathematical model of the inertial non-Newtonian fluid flow in the torus allowed to determine the conditions of homogeneity of the mechanical and thermal parameters in the flow domain and to develop method of viscosity measurement. The measured values are the shear rate on the inner surface of the capillary and the flow rate. The measurements are implemented with the computer vision system that processes data obtained from the high speed CMOS camera that records inertial flow in the transparent capillary illuminated with laser. The computer vision system is based on the application of deep convolutional neural network for laser speckle contrast imaging processing. During the experiments, the proposed viscometer was compared with the Brookfield rotational viscometer. The relative error of the proposed viscometer and method is less than 2%. The inertial viscometer is compact, it allows to study the wide range of shear rates per one test in automatic mode, and it has low fluid capacity of approximately 1.87 ml. That makes it possible to use the viscometer as a point on care testing device in medicine to study the rheology of physiological fluids, in particular blood.

1. Introduction

The viscosity of physiological fluids is one of the indicators for the diagnosis of various diseases. In particular, changes in blood viscosity could be associated with cardiovascular disease, diabetes, infectious diseases, anemia, various types of leukemia, etc. [1–3]. Blood is a multi-component solution with complex rheological characteristics. Whole blood is a non-Newtonian fluid [4]. From a rheological point of view, blood can be considered as a two-phase liquid, it can also be considered as a solid–liquid suspension, with the cellular elements being a solid phase. However, blood can also be considered as a liquid–liquid emulsion based on the liquid-like behavior of red blood cells under shear [5]. Blood is a predominantly shear thinning fluid [6]. This property has the most important non-Newtonian impact [7–10].

There are two main types of viscometers — capillary and rotational. The theory of a capillary viscometer corresponds to the Poiseuille flow and represents a steady viscous fluid flow under a pressure gradient between the two ends of a straight capillary [11,12]. The viscosity of a Newtonian fluid can be easily found from the equation of motion if the flow rate is measured. However, the shear rate across a capillary is not constant. Moreover, it is equal to zero at the center of a tube and is maximum on the surface [13]. The theory of a rotational viscometer corresponds to the Couette flow and represents a steady viscous fluid flow between two rotating coaxial cylinders [12,14,15]. The generalized Newtonian hypothesis [14,16] is used to determine the viscosity. The shear stress is determined by measuring the torque on the surface of one of the cylinders. It is assumed that the velocity distribution is

* Corresponding author.
E-mail address: lenoks_box@mail.ru (E.P. Kornaeva).

https://doi.org/10.1016/j.ijmecsci.2022.107967
Received 10 May 2022; Received in revised form 29 October 2022; Accepted 21 November 2022
Available online 30 November 2022

linear in the thin gap between the cylinders. Then the shear rate is constant across the gap thickness [17,18]. It is also assumed that the shear stress is uniform on the surfaces of the cylinders. For larger values of the radial gap between cylinders, the velocity can be found from the Navier–Stokes equation for Newtonian fluids. However, for example, the Brookfield viscometer is also used to measure the viscosity of non-Newtonian fluids [19]. An error of such measurements of viscosity for non-Newtonian fluids with a power-law (the Ostwald model $\mu(\xi) = \theta_0 \xi^{\theta_1 - 1}$) depends on the ratio of cylinders radii $\delta = r/R$ and the order of the power-law θ_1 [12]. As a result, the smaller the radial gap (i.e. $\delta \to 1$), the higher the accuracy. Thus, the viscosity can be determined from the generalized Newtonian hypothesis [14] of viscosity if the torque on the surface of a cylinder is measured.

Other types of viscometers, including diaphragm viscometers, falling body viscometers, microfluidic viscometers, vibrational and ultrasonic viscometers are easy to use, but have a number of significant assumptions [20]. So, their application to non-Newtonian fluids viscosity measurement is doubtful.

In general, the measurement of a non-Newtonian fluid viscosity is a challenging problem. The following challenges should be met [14,15,21]:

- the viscosity is usually a non-linear function that depends on shear rate, temperature and, in some cases, pressure;
- most viscometers measure some integral characteristics (flow duration, flow rate, torque, etc.), but the methods of viscosity measurement refer to the distributed values (shear rate, shear stress) that should have a uniform distribution or distribution functions should be known.

In this work, the authors improved the previously developed inertial method and viscometer [22] by applying a more accurate mathematical model of fluid flow and a modern computer vision system with the laser speckle-contrast imaging.

2. Literature review

As noted above, blood is a predominantly shear thinning fluid. Revellin et al. [23] investigated non-Newtonian properties of blood such as shear-thinning, viscoelasticity, thixotropy and yield stress. The authors showed that shear-thinning is the predominant non-Newtonian effect in blood flows. The non-Newtonian properties of blood occur in the range of shear rates from 1 to 200 1/s [13,16]. Meanwhile, Baskurt et al. [5] argue that blood exhibits pronounced non-Newtonian properties at shear rates up to 100 1/s and in the range from 100 to 200 1/s blood demonstrates weak non-Newtonian behavior. When the shear rate increases above 200 1/s, the blood viscosity does not change. The viscosity measurement results obtained for blood analogues of various concentrations demonstrate that the viscosity decreases in the range of shear rates from 1 to 100 1/s, and it is constant at the higher shear rates [9,18]. As a shear thinning fluid, blood is also characterized by a thixotropic behavior [7,9]. Thixotropy is more pronounced at low shear rates with a long time scale. However, this effect appears to have a less important role in blood flow than other non-Newtonian effects such as shear thinning [9,14]. Blood also demonstrates yield stress although it is a controversial issue [7,10,14]. Yield stress models can be useful to model blood flow in capillaries where flow at very low shear rates occurs [7,10].

Capillary and rotational viscometers, as well as falling body viscometers, are the most frequently used for blood viscosity measurements. For example, the Brookfield rotational viscometer with the UL adapter for low dynamic viscosity in the range from 1 to 10 mPa·s [19] allows measuring fluid viscosity as a shear rate function [17,18,24–27]. The test fluid capacity for this adapter is approximately 16 ml [19] which is a significant disadvantage. Gautam et al. [28] present a technique for measuring viscosity using a rotational viscometer for drilling fluids. The real-life drilling fluids are mostly non-Newtonian with a finite yield stress. This viscometer takes into account that the part of the fluid near the wall of the outer rotating cylinder moves as a solid body. In contrast to the Couette flow, the shear rate is supplemented by a term related to the true yield strength of the drilling fluids. Joye et al. [29] propose correction factors to calculate the shear rate when using a Couette-type viscometer with a small gap. These corrections are applicable in cases where the Casson model is used to describe the yield-stress pseudoplastic behavior of fluids. The correction factors tested in chocolate applications show very good agreement with viscosity–shear rate characteristics obtained with an "absolute" viscometer (cone-and-plate) at higher shear rates removed from the low shear rate unreliable data region. However, in this work, shear-thinning fluids are subject to study.

Capillary viscometers, falling ball and microfluidic viscometers require a smaller volume of fluid for tests. However, their disadvantage is the inability to control the shear rate during tests. Different shear rates can only be set by changing the capillary diameter or the flow rate. Lee et al. [30] present an analogue of a capillary viscometer equipped with a portable pump and a built-in pressure sensor. Oh et al. [31,32] present viscometers based on the Poiseuille flow. Several horizontal tubes of small capacity and different diameters are provided in the viscometers. As a result, several pairs of shear rate–viscosity points can be obtained in one test. Test results are presented for xanthan gum solution for shear rates from 150 to 900 s^{-1}, as well as blood in the shear rate range from 50 to 500 s^{-1} and 43% hematocrit. Shin et al. [33] discuss the application of a mass-detecting capillary viscometer (MDCV) to continuously measure the rheological characteristics of dairy foods over a range of shear rates by single measurement of liquid-mass variation with time. This MDCV can accurately measure non-Newtonian viscosity over a wide range of shear rates, extending as low as 0.1 s^{-1}. The obtained viscosities were compared with the data obtained with a rotating viscometer. The accuracy of the proposed device was demonstrated by measuring the viscosity of water and comparing the results with its reference value. Ferraz et al. [34] developed a tubular viscometer for apparent viscosity monitoring. The viscometer is based on volumetric fluid flow and pressure drop in a defined tube length. The proposed control method is based on Fuzzy Logic. Hapanowicz et al. [35] proposed a tubular rheometer for heterogeneous two-phase fluids. The authors demonstrated that the use of standard rotational rheometers could not require measuring possibilities for the water–oil system.

In the viscometers with falling body, different shear rates can only be set by changing the inclination angle. A cylinder and a ball are considered as falling bodies in some viscometers [36,37]. The Lovis viscometer with a falling ball in a thin glass capillary [38] has a test fluid volume of 0.1 to 0.8 μl. The duration of one measurement ranges from 30 s to 3 min. Yamamoto et al. [39] presented a similar viscometer with a falling needle. Sato et al. [40] designed a rolling ball viscometer for the simultaneous measurements of viscosity, density, and bubble-point pressure of CO_2-expanded fluids. Viscosity is calculated using the approximate equation of Hubbard and Brown [41] that is based on the time of passage of the ball, the angle of inclination of the viscometer, incremental change in temperature and pressure. The pass-through time was registered by the CMOS camera. Camas-Anzueto et al. [42] present an optical viscometer with a falling magnetic ball. Four mirrors are used to reflect the light beam onto the fluid three times. A ball falls under the force of gravity in a vertical column with fluid. The duration of the ball falling between two reference points is measured. The method for the viscosity calculation is based on an approximate formula in terms of the ball fall time, the density of the ball and the test fluid with a calibration factor. It should be noted that an additional disadvantage of falling body viscometers is that the shear rate distribution is not uniform on the surface of a falling body.

To date, there are several point-of-care diagnostic devices that are used for physiological fluids, in particular [16]. For example, the so-called microfluidic paper-based analytical devices (μPADs) [43] that

are inexpensive, easy to use, and specifically designed for applications in developing countries [44–46]. The Lucas–Washburn equation is used to measure viscosity in μPADs. However, the surface tension and contact angle must be known. In some cases a reference fluid of known viscosity is required. For example, Jang et al. [47] present a microfluidic paper-based viscometer for measuring the viscosity of biofluids such as urine, saliva, and plasma. The presented measurements results were compared with the results obtained by commercial viscometers. The viscometer requires a small volume of test fluid (20–100 μl) and does not require the use of reference fluids. However, as the authors point out, the application for non-Newtonian fluids is limited because the shear rate is not a controllable parameter and its value is taken as an average value depending on the flow rate and pore size of the material.

Mustafa et al. [25] proposed a viscosity measurement technique based on measuring the deflection of flexible (poly) dimethylsiloxane (PDMS) micropillars. A calibration curve of the reference fluid is used to determine the viscosity of an unknown fluid. Glycerol/water solutions of various concentrations were used as reference fluids. The authors showed a nonlinear relationship between the fluid viscosity and the deflection of the micropillars due to the viscoelastic properties of PDMS. The deflection of micropillars was recorded with a camera. Newtonian test fluids, such as n-decanol (11.91 cP) and aqueous glycerol (50 cP) solutions at the same flow (shear) rates used to generate the calibration curves (ranging between 15 and 60 ml/h) were used. Percentage error for 50 cP sample viscosity measurements was determined to be within 2.6–18.5%. The authors noted that on similar viscometers [48–50] for Newtonian fluids, errors of 3–10%, 4–7%, 5–24%, respectively, were obtained in comparison with commercial viscometers. Tzeng et al. [51] presented another microfluidic viscometer based on electrofluidic circuits. The viscosity of the tested fluid sample is estimated by its flow resistance, which is a function of pressure drop, flow rate, and the geometry of the microfluidic channel. The accuracy for the test fluid (glycerol/water solutions) depends on the concentration of the solutions and ranges from 0.1% to 8.9%. Given their low accuracy, the devices can probably be used for a qualitative assessment of the fluid properties. For example, for comparison with threshold values of blood viscosity to determine diseases. Khnouf et al. [52] proposed a PDMS microviscometer for Newtonian and non-Newtonian fluids. The viscometer is designed to measure the viscosity of the blood and requires less than 10 μl of test fluid. The test fluid is injected through the microfluidic channels at a predetermined flow rate using a syringe pump. An inverted microscope with a built-in camera was used to take snapshots of the fluid at different time steps. The height of the fluid column at each time step is measured for each image. Then the velocity is calculated. Viscosity is determined in terms of pressure drop, velocity, and channel size. The empirical model of viscosity is presented in the results in the form of a non-linear function of temperature, flow rate, and anticoagulant concentration. However, it was not taken into account that the fluid velocity is variable across the channel thickness and the dependence of viscosity on shear rate, and not on flow rate, is of interest. In addition, it is not clear how to determine the shear rate.

Falling ball viscometers, microfluidic viscometers and capillary viscometers are the simplest in use. Rotational viscometers are usually designed to control shear rates and some of them (Couette types with a small gap) provide a uniform shear rate or shear stress throughout the sample fluid [13,18]. Most of them may provide a relatively uniform temperature distribution, but none of them provide a uniform pressure distribution.

One of the ways to create a new type of viscometers, which combines the advantages of well-known viscometers and eliminates their disadvantages, is their combination. Previously, the authors presented the inertial viscometer, which is a hybrid of a rotational and a capillary viscometer with a capillary wrapped in a torus [22]. The method provides uniform distribution for the values of shear rate, shear stress, pressure and temperature on the surface of the capillary. The disadvantages of the proposed viscometer are the relatively large size of the device and a fairly rough assumption on the fluid velocity profile.

Dynamic light scattering methods are widely used in biomedical diagnostics, including assessment of blood flow, and allow for *in vivo* measurements [3,53–55]. McNamee et al. [56] authors applied purpose-built laser diffractometry in tandem with direct optical visualization to study blood shear flow and the effect of increasing in the red blood cells deformability under low-shear conditions. The laser speckle-contrast imaging (LSCI) method allows real-time visualization of microcirculation in tissues [57]. If moving scattering particles are present in the object illuminated by coherent light, then the blurring of the speckle image recorded by the camera will result in the observed standard deviation of the intensity being lower than for a completely static set of scatterers, and therefore the speckle image contrast will also be reduced. The average velocity of the scattering particles is inversely proportional to the characteristic correlation time of the intensity of the observed speckle dynamics [58]. The value of speckle-contrast correlates with the flow rate of the fluid in a capillary [59,60].

Computer vision methods allowed for high accuracy and excellent results in many areas [61]. Most of the methods are based on supervised learning [62]. The use of a private data set obtained from original physical experiments causes the following problems. Firstly, the data set is usually small that may affect overfitting during the training [62] and the low robustness of the trained model. The techniques of data augmentation using pretrained or low-complexity neural networks help to solve this problem partially [63–66]. Secondly, the data may have uncertainty [67–69] due to the factors of drift in the experimental environment and noise or errors in the measurement system. Predictions of an artificial neural network may also have uncertainty due to random initialization of the training and a set of hyperparameters of the network that affect the training results. Labeling of the data using the uncertainty class [70–73] and relabeling of the data during training [73], as well as the uncertainty estimation of the network predictions [67,74–77], allow to increase the accuracy of the artificial intelligence system.

Modern level of measuring instruments and modern methods of data processing based on machine learning make it possible to modify viscosity measurement methods.

3. Mathematical modeling

The section presents the mathematical model of fluid flow in a torus-shaped channel of the proposed inertial viscometer. On the basis of the dimensionless equations analysis of the mathematical model, the conditions for the homogeneity of the mechanical quantities distribution can be determined. The set of viscometer parameters can be determined on the basis of the analysis of the mathematical model and computational experiments.

3.1. Mathematical model of fluid flow in a torus-shaped channel

The unsteady flow of a viscous non-Newtonian incompressible fluid is studied. The flow domain is a torus-shaped channel (see Fig. 1). The torus radius is R and the capillary radius is r. The main equations are the Navier–Stokes equations, the continuity equation and the equation of convective heat conduction [78]. It is more convenient to present these equations in toroidal coordinates characterized with the Lame's coefficients [79]: $H_1 = 1$, $H_2 = \beta_1 \cos\beta_3 + R$, $H_3 = \beta_1$. As a result, the velocity field has only one non-zero component $\mathbf{V} = [[0\ \upsilon_2\ 0]]$ and the boundary conditions have a simple form. The continuity equation takes the trivial form: $\partial\upsilon_2/\partial\beta_2 = 0$. From the latter it follows that the velocity component υ_2 does not depend on the coordinate β_2 i.e. $\upsilon_2 = \upsilon(\beta_1, \beta_3)$. Since the fluid is pumped into the torus under some pressure p_0, then due to the symmetry of the flow domain, the pressure is a function of two coordinates $p = p(\beta_1, \beta_3)$. A detailed derivation of the

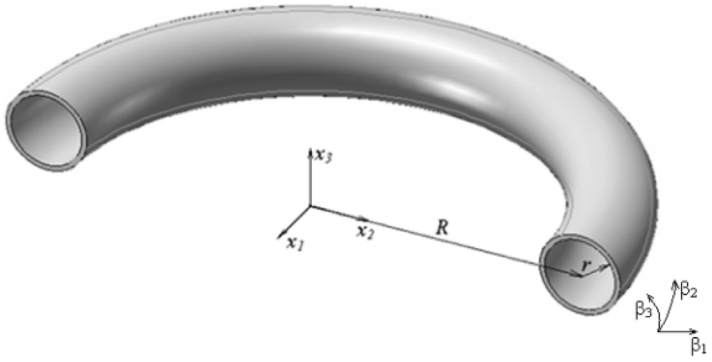

Fig. 1. Flow domain in a torus-shaped capillary.

mathematical model equations of fluid flow in the torus channel is presented in Appendix A.1.

To determine the conditions for the homogeneity of the pressure and temperature distributions, the equations of the mathematical model are presented in a dimensionless form. The dimensionless quantities were chosen so that the dimensionless coordinates and functions varied in the range $[0, 1]$. The dimensionless mathematical model equations of the considered fluid flow have the form (see Appendix A.2):

$$\widetilde{Eu}\frac{\partial\widetilde{p}}{\partial\widetilde{\beta}_1} = \frac{1}{\widetilde{H}_2+\gamma}\frac{\partial\widetilde{H}_2}{\partial\widetilde{\beta}_1}\widetilde{v}^2, \tag{1}$$

$$ShRe\frac{\partial\widetilde{v}}{\partial\widetilde{t}} = \frac{1}{\widetilde{H}_3(\widetilde{H}_2+\gamma)^2}\Big(\frac{\partial}{\partial\widetilde{\beta}_1}\big(\widetilde{H}_3(\widetilde{H}_2+\gamma)^2\widetilde{s}_{12}\big)+\psi\frac{\partial}{\partial\widetilde{\beta}_3}\big((\widetilde{H}_2+\gamma)^2\widetilde{s}_{23}\big)\Big), \tag{2}$$

$$\widetilde{Eu}\frac{\partial\widetilde{p}}{\partial\widetilde{\beta}_3} = \frac{1}{\widetilde{H}_2+\gamma}\frac{\partial\widetilde{H}_2}{\partial\widetilde{\beta}_3}\widetilde{v}^2, \tag{3}$$

$$ShRe\frac{\partial\widetilde{T}}{\partial\widetilde{t}} = \frac{1}{Pr}\frac{1}{\widetilde{H}_3(\widetilde{H}_2+\gamma)}\Big(\frac{\partial}{\partial\widetilde{\beta}_1}\big(\widetilde{H}_3(\widetilde{H}_2+\gamma)\frac{\partial\widetilde{T}}{\partial\widetilde{\beta}_1}\big)+\psi^2\frac{\partial}{\partial\widetilde{\beta}_3}\big(\frac{\widetilde{H}_2+\gamma}{\widetilde{H}_3}\frac{\partial\widetilde{T}}{\partial\widetilde{\beta}_3}\big)\Big)+ + 2Ec\widetilde{\mu}\big(\widetilde{\xi}_{12}^2+\widetilde{\xi}_{23}^2\big), \tag{4}$$

where $\widetilde{Eu} = p_0/(\rho V_0^2)$ is the Euler number analogue (hereinafter the Euler number); $Sh = r/(t_0V_0)$ is the Strouhal's number; $Re = V_0r/\eta_0$ is the Reynolds number; $Pr = \mu_0C_p/\lambda$ is the Prandtl number; $Ec = V_0^2/(C_p\Delta T)$ is the Eckert number; $V_0 = \omega R$ is the characteristic velocity; t_0 is the characteristic time of inertial fluid flow to stop; ΔT is the temperature change of the fluid; η_0 is the characteristic kinematic viscosity; ρ is the characteristic density.

The condition of pressure distribution homogeneity can be determined from Eqs. (1) and (3). The right hand sides of these equations are negligible compared to the pressure gradient components (the left-hand sides of the equations) when the following condition is true:

$$\widetilde{Eu} \gg \gamma^{-1}. \tag{5}$$

Eq. (5) helps to determine the flow velocity value V_0, while the values of the geometric parameter γ, the characteristic pressure p_0, and the fluid density ρ are given.

The first term on the right side of Eq. (4) corresponds to the internal heat transfer. The exponent of this term depends on the Prandtl number Pr and the dimensionless geometric parameter γ. The second term on the right side of Eq. (4) characterizes the heat transfer due to forced convection. The exponent of this term depends on the Eckert number Ec. The order of the left side of Eq. (4) depends on the Strouhal number Sh and the Reynolds number Re. Thus, it is possible to achieve homogeneity of the temperature distribution in the flow channel by imposing the following condition:

$$ShRe \gg max(Pr^{-1}; Ec). \tag{6}$$

Eq. (6) determines the conditions under which the terms on the right side of the Eq. (4) are negligible compared to the left side of the equation. The exponent of the Reynolds number Re is determined from condition Eq. (5) for a fixed value of the capillary radius r and the characteristic viscosity η_0. The Prandtl number Pr is determined from the properties of the fluid. For example, for blood, it varies in the range 2.72–3.55 [80]. The Eckert number Ec depends on the characteristic velocity determined by Eq. (5), as well as on the value of ΔT. Therefore, when estimating its exponent, the condition of an insignificant temperature difference was taken into account 10^{-1} °C. Eq. (6) determines the exponent of magnitude of the characteristic time of the inertial fluid flow in the considered channel. Thus, it is possible to determine the conditions for the homogeneity of the pressure and temperature distributions from Eq. (5) and (6).

Fluid flow in the torus can be initiated due to inertia. If the torus rotates at a constant angular velocity, then the fluid inside the torus moves like a quasi-rigid body. But if the torus stops, the fluid continues to flow for some time. It is possible to determine the torus velocity before stopping Eq. (5) and the fluid flow duration after the torus stops Eq. (6). To neglect the curvature of the channel along the coordinate $\widetilde{\beta}_2$, the condition $R \gg r$ or $\gamma \gg 0.5$ must be satisfied. Taking into account this condition and Eq. (5) and (6), Eq. (2) can be transformed into the following form (see Appendix A.2):

$$ShRe\widetilde{\beta}_1\frac{\partial\widetilde{v}}{\partial\widetilde{t}} = \frac{\partial}{\partial\widetilde{\beta}_1}(\widetilde{\mu}\widetilde{\beta}_1\frac{\partial\widetilde{v}}{\partial\widetilde{\beta}_1}). \tag{7}$$

3.2. Numerical solution for a non-Newtonian fluid flow

It is more convenient to present Eq. (7) in a dimensional form to determine the velocity distribution:

$$\beta_1\frac{\partial v}{\partial t} = \frac{\partial}{\partial\beta_1}(\eta\beta_1\frac{\partial v}{\partial\beta_1}), \tag{8}$$

where $v = v(\beta_1)$ is an axial velocity component; η is kinematic viscosity.

The initial and the boundary conditions have the following form:

$$v(0,\beta_1) = V_0,\ v(t,r) = v_t(t),\ \frac{\partial v(t,\beta_1)}{\partial\beta_1}\Big|_{\beta_1=0} = 0. \tag{9}$$

Dynamic viscosity is a function of shear rate and can be represented by the Ostwald model [15]:

$$\mu(\xi) = \theta_0\xi^{\theta_1-1}, \tag{10}$$

where θ_0, θ_1 are the model parameters; $\theta_1 < 1$ for pseudoplastic fluid, in particular blood [14].

A density value does not depend on the shear rate. Therefore, it is constant at a fixed test temperature. Given the above, it is possible to determine the kinematic viscosity as a function of the shear rate $\eta(\xi)$.

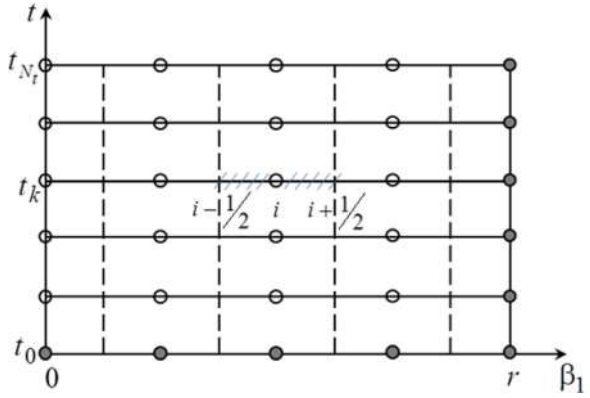

Fig. 2. Control volumes in the time and space domain. Filled markers mean that the boundary conditions are set. Unfilled markers indicate calculated points with unknown values. Dashed lines indicate one-dimensional control volume.

It is convenient to use the control volume method (CVM) to solve Eq. (9). The method allows using a small number of calculation points, unlike other grid methods [78]. The scheme for the discretization of the calculation domain is shown in Fig. 2

Eq. (8) is integrated over each control volume (CV) $[\beta_{1\,i-1/2}, \beta_{1\,i+1/2}]$. The velocity gradient component $\partial v/\partial\beta_1$ on the right side of Eq. (8) at points $\beta_{1\,i-1/2}$ and $\beta_{1\,i+1/2}$ is replaced with the corresponding central finite differences. On the left side of Eq. (8) the first mean value theorem for definite integrals is used when integrating over β_1. And the partial derivative with respect to time is replaced with the right finite difference. As a result, a system of linear algebraic equations is obtained for the velocity at each calculated point in coordinate and time:

$$a_i^k v_{i+1}^{k+1} + b_i^k v_i^{k+1} + c_i^k v_{i-1}^{k+1} = -d_i v_i^k, \tag{11}$$

where $i = 1,..N_r - 1$ corresponds to the spatial coordinate; $k = 1,..N_t$ corresponds to time.

The initial velocity and the boundary values, respectively:

$$v_i^0 = V_0,\ v_{N_r}^k = v_t(t^k),\ v_0^k = v_1^k, \tag{12}$$

$$a_i^k = (\frac{\beta_{1i}}{\Delta\beta_1} + \frac{1}{2})\eta(\xi_{i+1/2}^k),\ c_i^k = (\frac{\beta_{1i}}{\Delta\beta_1} - \frac{1}{2})\eta(\xi_{i-1/2}^k), \tag{13}$$

$$d_i = \frac{\Delta\beta_1}{\Delta t}\beta_{1i},\ b_i^k = -a_i^k - c_i^k - d_i, \tag{14}$$

where $\eta(\xi_{i+1/2}^k)$ is the value of the kinematic viscosity in the previous time step t_k; $\xi_{i+1/2}^k = (v_{i+1}^k - v_i^k)/(2\Delta\beta_1)$, $\xi_{i-1/2}^k = (v_i^k - v_{i-1}^k)/(2\Delta\beta_1)$.

The computational experiment on model Eqs. (11)–(14) was carried out at different values of the torus rotation frequency. The characteristic dimensions of the torus are R=0.095 m and r = 0.001 m. The pressure in the torus is p_0=0.1 MPa. The values of the torus rotation frequency n=50–200 rpm were obtained from Eq. (5): $V_0^2 \ll p_0\gamma/\rho$. Numerical solutions were obtained for the three types of fluids: blood $\mu(\xi) = 0.0115\xi^{-0.199}$ [14], Intralipid $\mu(\xi) = 0.01\xi^{-0.282}$, and a solution of Intralipid with glycerol $\mu(\xi) = 0.036\xi^{-0.018}$.

Fig. 3 demonstrates plots of the shear rate in time, obtained from the numerical solution of Eqs. (8), (9) or Eqs. (11), (12). Fig. 3(a) demonstrates plots of the shear rate in time for blood flow in the channel at various initial torus rotation frequencies range n=50–200 rpm. Fig. 3(b) shows graphs of the shear rate over time at the frequency of n=100 rpm for the three types of fluids. It can be seen in Fig. 3(a) that the fluid flow duration (after the torus has stopped) does not depend on the torus initial velocity. However, Fig. 3(b) shows that the flow duration depends on the kind of fluid. The fluid flow lasts less than half a second at given geometric static and thermomechanical parameters. The obtained results fully comply with the requirements of Eq. (6). Therefore, the choice of the initial rotation frequency of the torus should be made based on the dimensionless similarity criteria (see Eq. (5)).

4. Inertial viscometer with a computer vision system

The proposed viscosity measurement method was implemented in a compact test setup with widely available components.

The three-dimensional model of the test setup is shown in Fig. 4. Fig. 5 shows the structural and functional diagram of the test rig. Some of the details of the test setup were made of PLA plastic using a 3D printer. The torus is made of nylon. The disc is mounted to the stepper motor using an aluminum flange coupling. The disc has slots for tube connectors. The sizes of the torus and capillary are: R = 0.095 m, r = 0.001 m. The tests have the following order of actions. The test fluid with light-reflecting particles is pumped into the torus under pressure p_0. The disk has been smoothly accelerated by the stepper motor up to the rotation frequency n, then stopped immediately. The brake helps stop the disc and prevent the disk vibrations. Thus, after the torus stops, the fluid flow inside the torus is investigated, which continues for some time.

The initial torus speed is determined by Eq. (5): $V_0^2 \ll p_0\gamma/\rho$. In theory (see Section 3.2), the fluid flow duration t_0 does not depend on the initial torus speed, but it depends on the type of fluid. The torus rotation frequency range n=50–200 rpm provides the values of the shear rates range that corresponds to the natural shear rates of the blood in a human body.

During the inertial fluid flow, the computer vision system registers and processes a sequence of images of the fluid flow. The fluid flow is illuminated by a laser module through a biconcave lens. Images of fluid flow are captured by a CMOS camera through a lens. The received images are processed by the Jetson Nano mini-computer, the calculations are accelerated using the mini-computer CUDA cores.

The expansion board for the Jetson Nano mini-computer is shown in Fig. 5 at position 2. The expansion board allows to reduce the computing load on the mini-computer, as well as simplify the setup of the installation. The functions of the board include: stepper motor control via the STEP/DIR interface, digitization of the signals from the temperature sensor and laser module power control. The board is based on the STM32G071 micro controller. The controller has the necessary set of peripherals. To control the stepper motor, the DRV8825 stepper motor driver is used as a part of the module. The module is applicable for controlling the stepper motors with winding current up to 2 A. B57861S0103F040 thermistor connected to the analogue to digital converter of the micro controller. Communication between the main controller and the board is carried out via the UART interface. The output power of the laser module is adjusted by the resistor of the expansion board.

5. Experimental studies and results

This section presents the design and the results of an experimental study of the viscosity of non-Newtonian fluids. The technique to measure the viscosity by the proposed inertial viscometer includes the following stages (Fig. 6, Section 5.3): (1) obtain a sequence of images of the inertial fluid flow in the torus; (2) predict the flow rate and the shear rate at each time step; (3) calculate the kinematic viscosity of the fluid at each time step using the Navier–Stokes equation (8). The shear rates and the flow rates are predicted using the deep neural network. The data for training were obtained using an additional experiment (Fig. 6, Sections 5.1 and 5.2).

5.1. Training data for the computer vision system

The Intralipid solution of 20% (SMOFlipid, Austria) with glycerol was used as the test fluid. The dynamic viscosity of the test fluid at various shear rates and constant temperature T=25.5 °C is presented

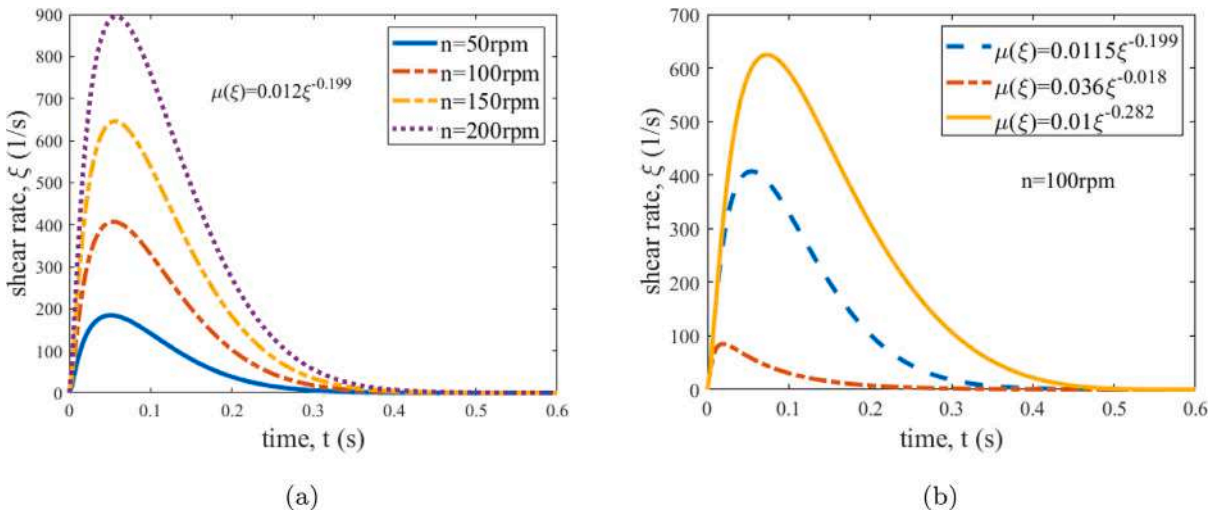

Fig. 3. The results of the fluid flow simulation obtained for the torus of size R=0.095 m, the capillary radius is $r = 0.001$ m: the shear rate as the function of time at different initial torus rotation frequency and for the blood viscosity model $\mu(\xi) = 0.0115\xi^{-0.199}$ (a); the shear rate as the function of time regarding different kinds of fluids at a constant initial torus rotation frequency n=100 rpm (b).

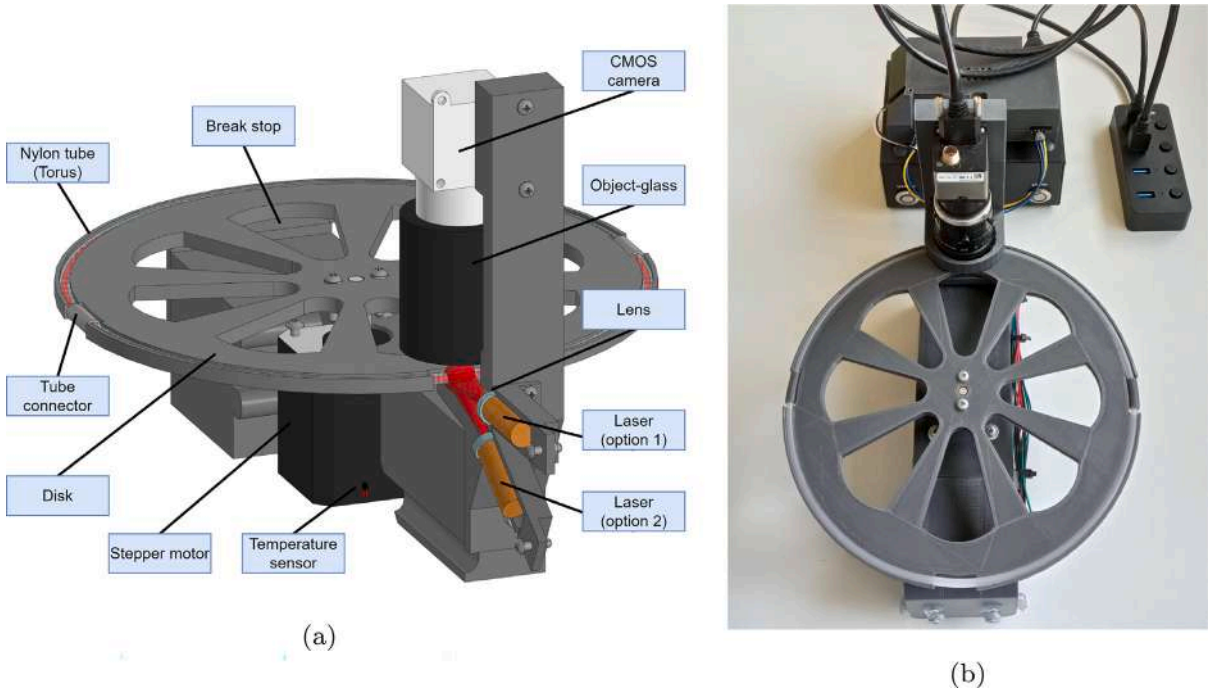

Fig. 4. Overview of the experimental setup: the 3d model (a) and the photograph of the test rig (b).

in Fig. 7 . The results are presented as the average values of the viscosity for five parallel tests. Measurements were taken on the Brookfield DV-II+Pro viscometer with a UL cylinder-to-cylinder spindle used for low-viscosity fluids. According to the measurement results, it can be seen that the test fluid has pseudoplastic properties due to the non-Newtonian properties of Intralipid. The data obtained were used to estimate the accuracy of the new method.

The data set with labels to train the computer vision system was obtained experimentally. The test fluid was pumped through a long transparent capillary of radius $r = 0.001$ m. The flow rates were controlled by an electric pump and established according to the required shear rates range. The enforced flow of a viscous fluid in a tube is known as the Poiseuille flow [12,21] and the task has a known analytical solution. Therefore, the relationship between the flow rate and the shear rate given on the inner surface of the capillary can be expressed with one formula:

$$Q = \frac{\pi r^3}{2}|\xi_r|,$$

where r is the capillary radius; $|\xi_r|$ is the shear rate on the inner surface of the capillary.

The plan of the experiment included 19 pairs of the shear rate ξ and the flow rate Q in the ranges of 7–117.5 1/s and 39.8–663.6 ml/h, respectively. A set of 5 parallel tests was carried out for each pair of ξ_i and Q_i. The video recording time was 20 s for each test. A total of 95 tests were carried out. The CMOS camera recorded the video of the fluid flow inside the transparent capillary with illumination by a 650 nm diode laser. Thus, an ith labeled sample $\{\mathbf{X}_i, \xi_i, Q_i\}$ included the sequence of images $\mathbf{X}_i$, the corresponding shear rate ξ_i and flow rate Q_i. The images were preprocessed using the LSCI method. This

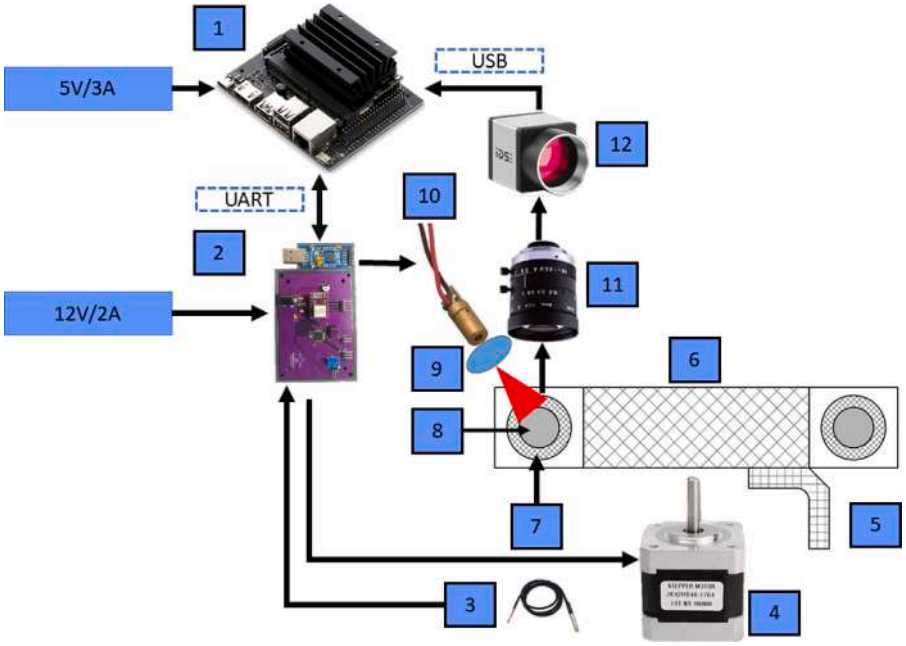

Fig. 5. Structural and functional diagram of the inertial viscometer. Mini-computer Jetson Nano (1) is the main controller of the test rig. Expansion board (2) controls 17HS4401 stepper motor (4) and laser module (10). Temperature sensor (3) controls the overheating. Data transmission between (1) and (2) is implemented using the UART protocol. The torus (7) is fixed on the disc (6). Test fluid (8) is injected into the torus (7). Lens (9) dissipate the coherent light of the laser module (10) into the test fluid (8). Brake stop (5) prevents the disc vibrations (6). IDS UI-3220CP-M-GL CMOS camera (12) with AZURE-0814M3M camera lens (11) acquires fluid flow sequence of images and implement the LSCI method. The CMOS camera (12) transmits data to Mini-computer Jetson Nano (1) via USB interface.

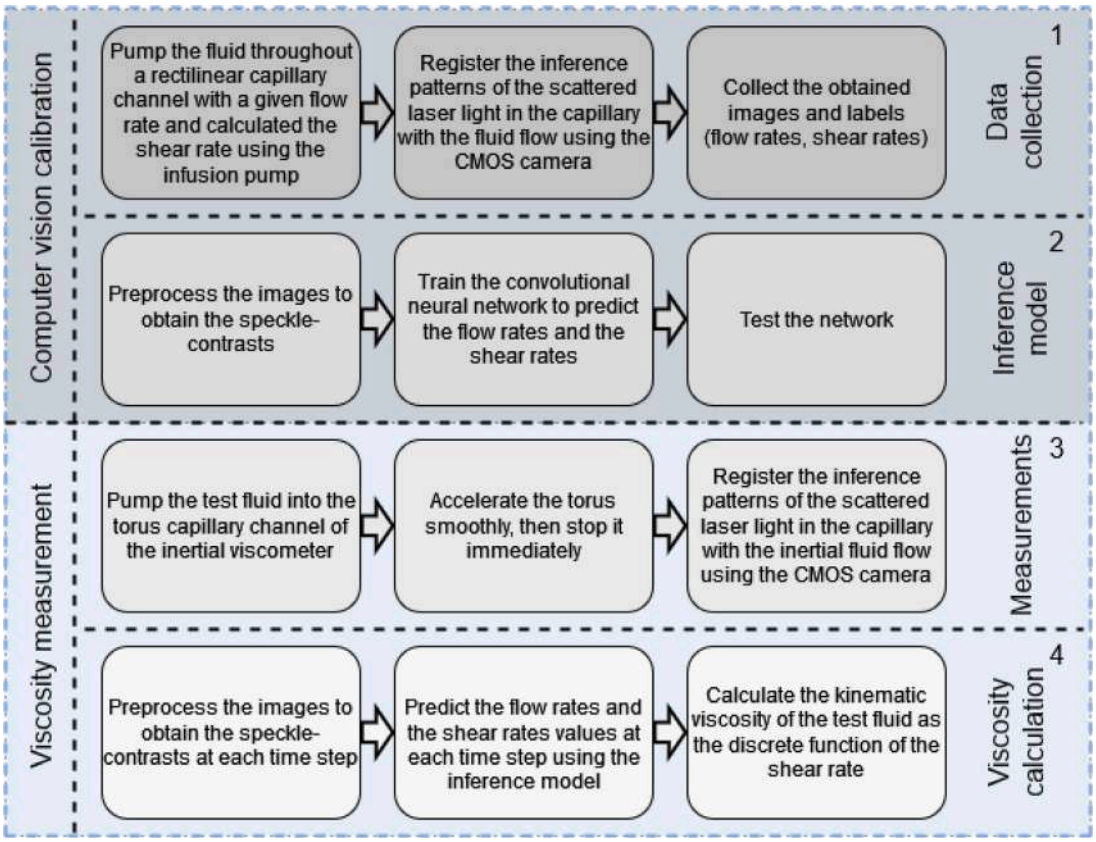

Fig. 6. The proposed viscosity measurement method intuition. The method is based on the computer vision system that can be trained to recognize the flow rate and the shear rate of the fluid flow in the transparent capillary (lines 1 and 2). The computer vision system analyzes the inertial flow of the test fluid in the torus capillary and recognize the flow rate and the shear rate at each time step of the inertial flow. Then the viscosity values are calculated at the each time step.

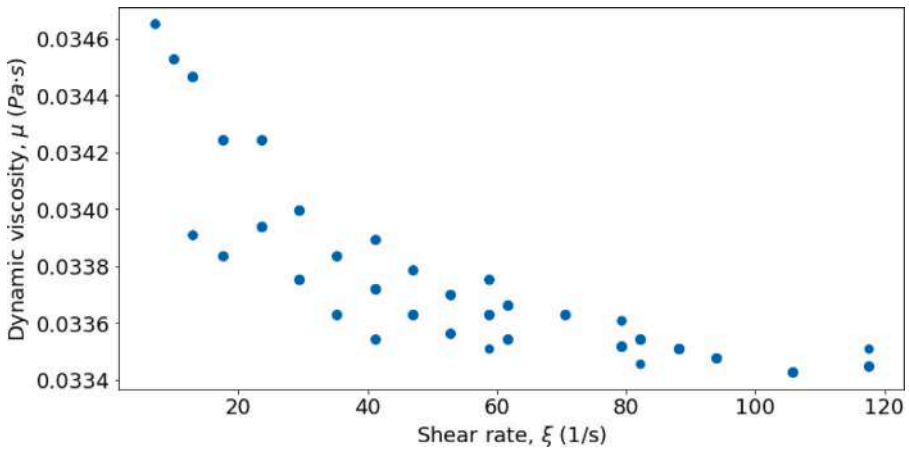

Fig. 7. Viscosity of the intralipid solution of 20% (SMOFlipid, Austria) with glycerol at the different shear rates and constant temperature T=25.5 °C. Viscometer: the Brookfield DV-II+Pro with a UL cylinder-to-cylinder spindle used for low-viscosity fluids.

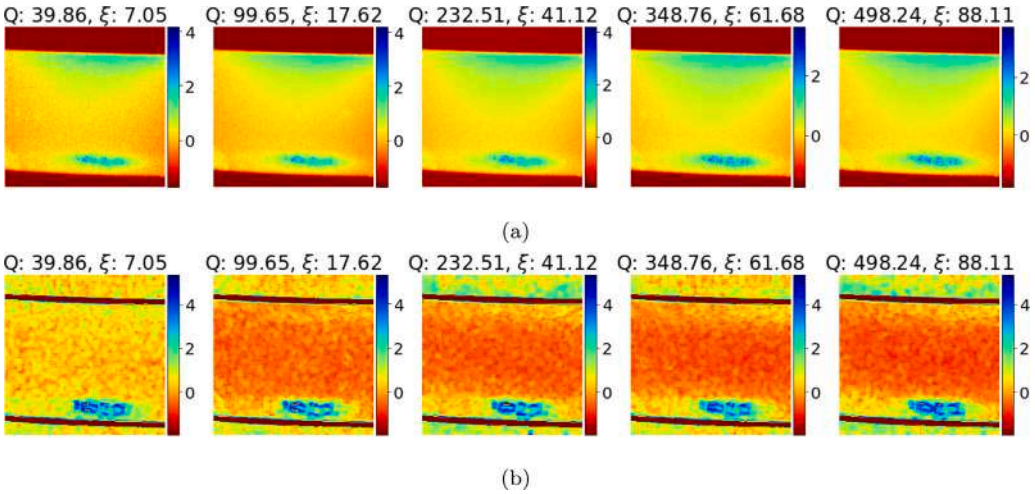

Fig. 8. Random frames of the training data set in the form of images with labels of corresponding values of the flow rate Q and the shear rate ξ: the original images (a); the images processed by spatial speckle contrast method (b).

method allows one to obtain an image of dynamic inhomogeneities by analyzing the local speckle-contrast [58]. When the scattering fluid is illuminated with coherent light, a random picture of the light intensity arises. This pattern is caused by interference within the fluid and at its surface. The resulting intensity structure is known as a speckle pattern. The movement of particles in the fluid leads to blurring in the image due to averaging over the exposure time of the camera. Spatial and temporal statistics of speckle patterns are used to extract information on motion in fluids under study. Spatial speckle-contrast (SSC) is calculated in a small square area of an image. The optimal size for this area is a 7 × 7 pixels window [53]. This window moves horizontally and vertically across the image. The spatial speckle-contrast in each window is calculated with formula:

$$K = \frac{\sigma_n}{\langle I_n \rangle}, \tag{15}$$

where n is subdomain size; σ_n is intensity standard deviation; $\langle I_n \rangle$ is mean intensity.

To implement the LSCI method, a CMOS camera IDS UI-3220CP-M-GL was used (see Figs. 4, 5). To ensure recognition at a high flow rate, the camera operated at a maximum frequency of 240 FPS and an exposure time of 0.1 ms. In addition, high frequency allows to receive more data in a certain time. A high speed of image acquisition is also required to study the inertial flow, since such a flow is characterized by the time of less than 1 s. To ensure the stable operation of the software, the transfer of images from the camera to the mini-computer and their recording to the hard disk occur in an asynchronous mode. To save computational resources, the camera transmits only a 224 × 224 pixels fragment of the fluid flow domain. For maximization of the signal-to-noise ratio, the minimal speckle size must exceed the Nyquist criterion [81]. Thus, the speckle size on the camera was adjusted by changing the pupil diameter of the camera lens to achieve a speckle size at least 2 times the pixel size. The speckle size can be estimated using the equation [81]: $S = 2.44\lambda(1 + M)f/\#$, where λ is the illumination wavelength, M is the imaging system magnification, and $f/\#$ is the camera lens aperture.

Fig. 8 demonstrates the original images and the spatial speckle contrast images at various flow rates. Fig. 9 shows diagrams of the distribution of the spatial speckle-contrast at the different values of the shear rate and the flow rate.

The correlation of speckle contrasts and kinematic characteristics of the flow makes it possible to develop models and tools to predict the shear rate and flow rate from the speckle contrast images.

5.2. Training and test the computer vision system

Experimental data for enforced flow in a capillary were applied to train artificial neural networks (ANNs) that approximate the flow rate and the shear rate from the speckle-contrast values. Two ANN

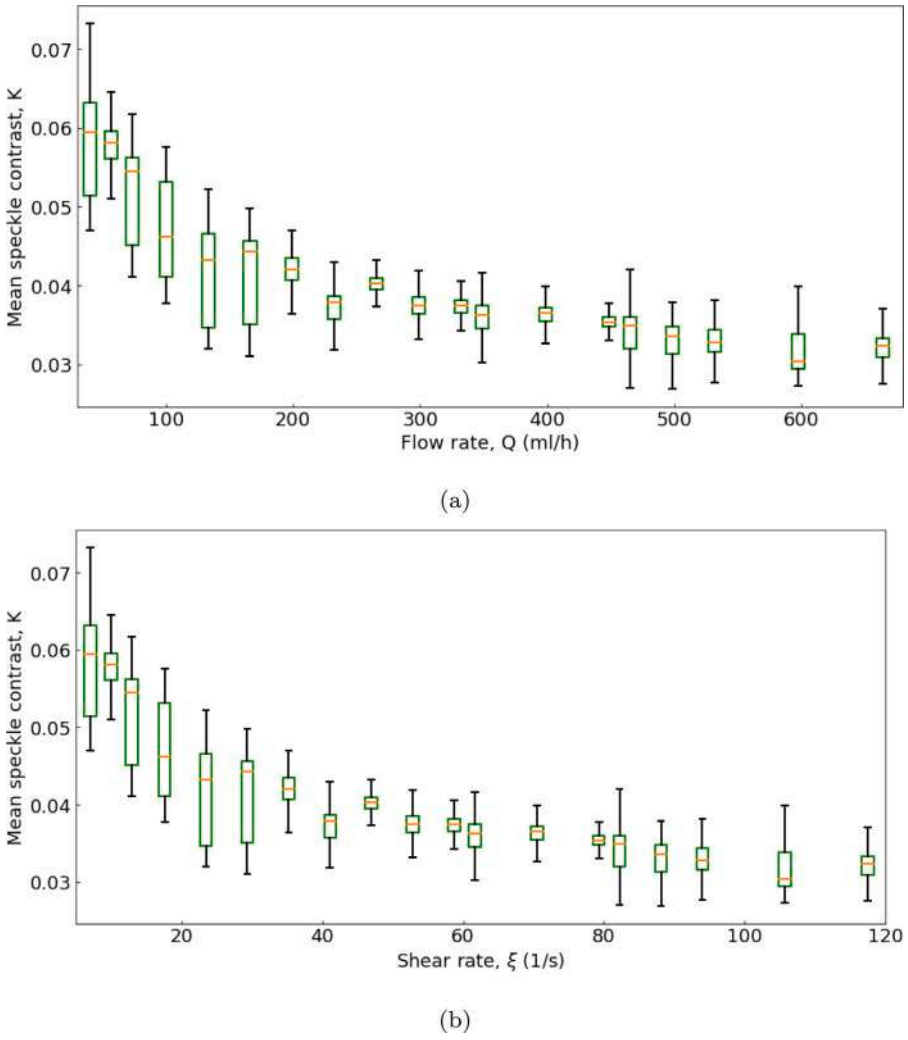

Fig. 9. The average spatial speckle contrast distribution depends on the flow rate (a) and the shear rate (b). The diagrams show that with an increase in the flow rate and the shear rate, the speckle contrast decreases nonlinearly. Also, there may be no significant difference between neighboring flow rates and shear rates, which makes it difficult to determine them only by the speckle contrast value. As a result, neural networks will be used for regression.

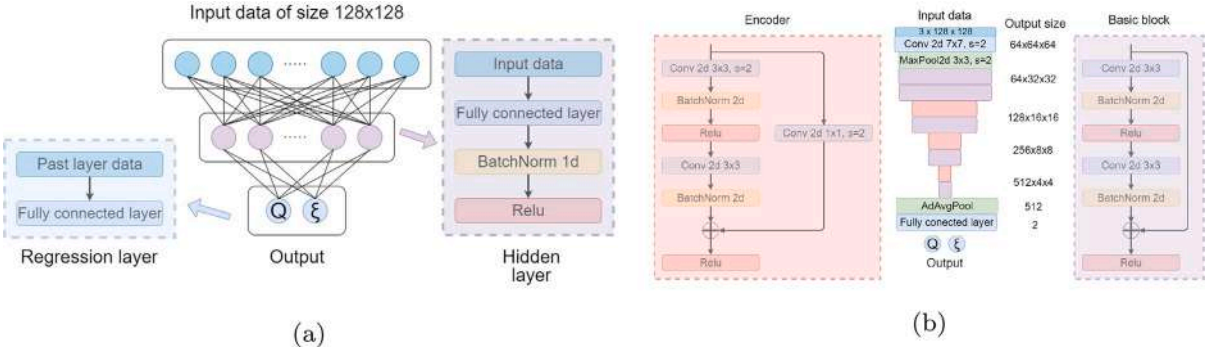

Fig. 10. The proposed neural network architectures are MLP (a) and ResNet18 (b). The MLP processes the input image as a series of independent features. The ResNet18 is able to find specific objects in an image and identify the most important features, which helps to increase the ability of the network to generalization of the obtained data.

Table 1
Metric values.

	Training			Validation			Testing		
Model	MSE	$R^2(Q)$	$R^2(\xi)$	MSE	$R^2(Q)$	$R^2(\xi)$	MSE	$R^2(Q)$	$R^2(\xi)$
MLP_1	0.395	0.792	0.792	0.916	0.172	0.173	0.826	0.270	0.270
MLP_2	0.0494	0.981	0.981	0.0630	0.950	0.950	0.0745	0.948	0.948
CNN_1	0.005	0.998	0.998	0.3941	0.630	0.630	0.4032	0.635	0.635
CNN_2	0.0222	0.996	0.997	0.0613	0.958	0.957	0.0739	0.956	0.960

Table 2
Metrics of the proposed method for the test fluid with non-Newtonian properties.

Shear rate ranges, 1/s	RSD, %	ε_{max}, %	$\bar{\varepsilon}$, %
(0; 20)	1.603	2.014	1.309
(20; 40)	0.6041	1.437	0.5817
(40; 60)	0.1306	0.6885	0.2189
(60; 80)	0.1166	0.1995	0.1498
(80; 100)	0.08747	0.2651	0.07419
(100; 120)	0.1735	0.2249	0.1803

architectures were used: a multilayer perceptron (MLP, see Fig. 10(a)) and the ResNet18 convolutional neural network (CNN, see Fig. 10(b)). Two options for data preprocessing were used: normalization of the original images and image processing by the LSCI method (see Eq. (15)) with normalization. The mean square error (MSE) was applied as the loss function:

$$MSE = \frac{1}{2n}\sum_{k=1}^{2}\sum_{i=1}^{n}\left({y_{true}}_i^{(k)} - {y_{pred}}_i^{(k)}\right)^2 \rightarrow min \tag{16}$$

where n is the number of samples in the training dataset; ${y_{true}}_i^{(k)}$ are true (target) values (ξ_i and Q_i); ${y_{pred}}_i^{(k)}$ are predicted values.

To solve the optimization problem Eq. (16), the values of the flow rate Q_i and the shear rate ξ_i were normalized. Subsequently, when presenting the results, all values were converted back to the dimensional form. The Adam optimizer [82] was used to train the models. The data set was divided into three subsets for training, cross-validation and test, respectively. Cross-validation was carried out for 4 folds [62]. The training step was set as a hyperparameter for the models (Fig. 10) with the following values $[10^{-4}, 5\cdot10^{-4}, 10^{-3}, 5\cdot10^{-3}, 10^{-2}, 5\cdot10^{-2}, 10^{-1}]$. An additional hyperparameter was the number of neurons in the hidden layer of the MLP with the following values $[16, 32, 64, 128]$. For ResNet18, an additional hyperparameter was the number of neurons in the fully connected layer in the range $[64, 128, 256]$. ResNet18 was pre-trained on the well-known ImageNet dataset, as well as on the data presented in the work [59]. MSE and the coefficient of determination R^2 metrics are presented in Table 1 for MLPs and CNNs: with the original images (MLP_1, CNN_1) and the SSC images (MLP_2, CNN_2).

The optimal result in validation and test was obtained for the ResNet18 (CNN_2, see Table 1) network that was trained on SSC images using a pre-trained neural network from [59] and without using an additional fully connected layer (see Fig. 10(b)).

Thus, the ResNet18-based model, trained and optimized on the SSC images, predicts the values of the flow rate and the shear rate on the inner surface of the capillary with high accuracy. The next subsection demonstrates that, based on predicted kinematic characteristics, it is possible to calculate the value of the kinematic viscosity by numerical solution of the Navier–Stokes equation Eq. (8).

5.3. Proposed viscosity measurement method

According to Eq. (8), the viscosity distribution correlates with the velocity distribution. After the integration across the β_1 coordinate and taking into account the boundary conditions $\eta|_{\beta_1=0} = \eta_0$ and $\frac{\partial v}{\partial \beta_1}\Big|_{\beta_1=0} = 0$, Eq. (8) takes the following form:

$$\int_0^{\beta_1} \beta_1 \frac{\partial v}{\partial t} d\beta_1 = \left(\eta\beta_1 \frac{\partial v}{\partial \beta_1}\right)\Big|_{\beta_1} - \left(\eta\beta_1 \frac{\partial v}{\partial \beta_1}\right)\Big|_{\beta_1=0}$$

The above equation is written on the inner surface of the capillary of the torus $\beta_1 = r$. After some transformations on the left side of the equation, replacing $\int_0^r \beta_1 v d\beta_1 = \frac{Q}{2\pi}$ the following is obtained:

$$\frac{\partial Q}{\partial t} = 4\pi r \xi_r \eta_r,$$

where $\xi_r = \frac{1}{2}\frac{\partial v}{\partial \beta_1}|_{\beta_1=r}$ is the shear rate on the inner surface of the capillary of the torus; η_r is the kinematic viscosity on the inner surface of the capillary (hereinafter η); Q is the flow rate.

The derivative on the left side of the equation was approximated by a finite difference method. Then the kinematic viscosity was determined in terms of the shear rate and flow rate at each time step t^k:

$$\eta^k = \frac{1}{8\pi r \Delta t}\frac{4Q^k - 3Q^{k-1} - Q^{k+1}}{\xi_r^k}, \tag{17}$$

where ξ_r^k, Q^k are the shear rate on the inner surface of the capillary and the flow rate at each time step t^k, respectively; $\Delta t = t^{k+1} - t^k$ is the constant time step value.

Taking into account the pre-trained ResNet18 model (see Section 5.2), the automated kinematic viscosity measurement algorithm includes the following steps:

(1) receive the data on the inertial fluid flow in the torus of the viscometer in a form of the sequence of images obtained during the time interval t_0 with the time step Δt;

(2) predict the shear rate ξ^k at the inner surface of the capillary and flow rate through the capillary Q^k of the torus at each time step t^k using the ResNet18 inference model (Section 5.2);

(3) calculate the kinematic viscosity values as a function of shear rates ξ^k using Eq. (17).

5.4. Results and discussion

Comparison of the predicted and target values of the flow rates and the shear rates is shown in Fig. 11. Fig. 12 demonstrates graphs of the average temporal speckle contrast for the inertial fluid flow in the torus after the torus rotated at the speed of 50 rpm has stopped. The data were averaged over 10 tests and filtered.

Therefore, during the measurement period of time t_0, an array of values of the shear rate and the corresponding values of the kinematic viscosity were determined. Fig. 13 demonstrates the flow rates and shear rates predicted by the CNN inference model (see Section 5.2) for 10 parallel tests at the initial torus speed of n=50 rpm. The values were approximated by exponential functions of time.

The predicted flow rates and shear rates were then used to calculate the kinematic viscosity using Eq. (17). Fig. 14(a) demonstrates the dynamic viscosity calculation results $\mu(\xi) = \rho\eta(\xi)$ using the proposed method and also shows the values of dynamic viscosity measurements on the Brookfield rotational viscometer (test sample, see Section 5.1). Table 2 presents metrics of the measurement accuracy according to the proposed method for the test fluid with non-Newtonian properties. The data obtained from the Brookfield viscometer (see Section 5.1) were applied as gold standard. The metrics were calculated for different intervals of the shear rates. The relative standard deviation (RSD, %) and mean relative error ($\bar{\varepsilon}$, %) were calculated as metrics. The relative error distribution is shown in Fig. 14(b). The minimum error and the minimum standard deviation are provided at high shear rates. The maximum average relative error in the range of shear rates $0 < \xi < 20, 1/s$ was about 2%.

Additional experiments were carried out on a Newtonian fluid to assess the accuracy of the measurements on the presented viscometer. Zinc oxide suspension (0,1%) in 80% aqueous glycerol solution was used as the test fluid. The particle size of the zinc oxide powder was about 400 nm. Zinc oxide powder was added to the test fluid

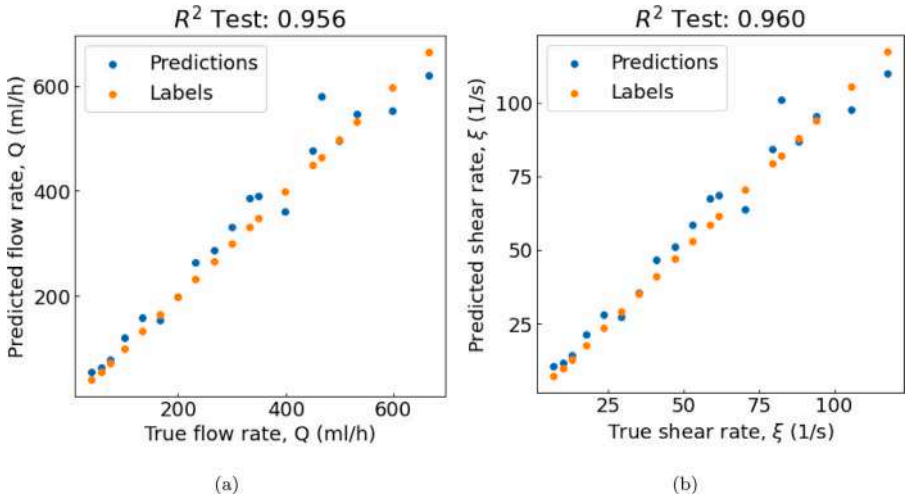

Fig. 11. The values predicted by the network are compared with the target values: the predicted (blue markers) and target (orange markers) values of the shear rates (a) and the flow rates (b). Evaluation of the accuracy of the predictions is based on the data from the test set. The determination coefficient is applied to estimate the quality of the predictions which is 0.956 and 0.96, respectively.

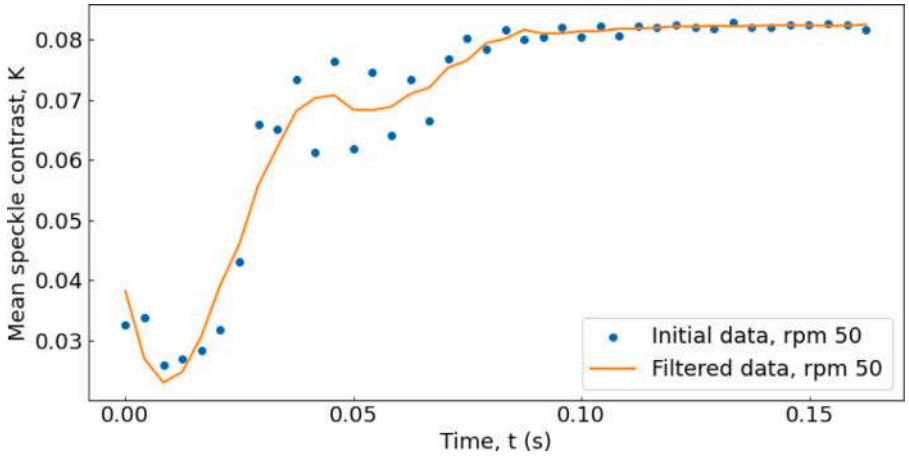

Fig. 12. Average temporal speckle contrast values in time for the inertial fluid flow in the torus after the torus rotated at the speed of 50 rpm has immediately stopped. The interval from 0.02 s to 0.04 s corresponds to a gradual increase in the speckle contrast value. Beyond this interval, the speckle contrast value is not sensitive to changes in the flow velocity.

as reflective light particles to enable the LSCI method to be applied. Before each test, the test fluid was stirred in an ultrasonic bath to improve the uniformity of the reflective particles. Measurements of the viscosity of the test fluid by the Brookfield viscometer showed the independence of viscosity from shear rate (blue dot markers in Fig. 15(a)). Thus, the addition of zinc oxide powder at the presented concentration did not affect the linearity of the fluid properties. And also, the viscosity value of the suspension corresponds to the reference value of the viscosity of 80% aqueous glycerol solution. Fig. 15(a) shows the results of measuring the test fluid viscosity by the Brookfield viscometer and using the proposed methodology. The measurements were carried out at a temperature of 25 °C. The measurement results were compared with the reference value of viscosity for 80% glycerol solution ($\mu = 0.04586$ Pa s).

Table 3 presents the values of the measurement errors of the Brookfield viscometer. The RSD errors and the average relative error are presented relative to the reference value. Table 4 presents the same metrics to estimate the error of the proposed method. The RSD and the $\overline{\varepsilon}$ metrics for the proposed method are less than 0.5% and decrease with increasing shear rate (Fig. 15(b)). The error of the method is comparable to the error of the Brookfield viscometer. It is worth noting that Brookfield measurements are sensitive to the shear rate, as stated in the instructions. The error of the presented method is less sensitive to the shear rate. However, in this case, these remarks are unimportant due to the small error.

Table 3
Error of the Brookfield viscometer measurements of the test Newtonian fluid.

Shear rate ranges, 1/s	RSD, %	ε_{max}, %	$\overline{\varepsilon}$, %
(0; 20)	0.1396	0.6254	0.4430
(20; 40)	0.1267	0.3834	0.1425
(40; 60)	0.1019	0.2013	0.1022
(60; 80)	0.0849	0.1406	0.0678
(80; 100)	0.0325	0.325	0.0325

Table 4
Error of the proposed measurement method of the test Newtonian fluid.

Shear rate ranges, 1/s	RSD, %	ε_{max}, %	$\overline{\varepsilon}$, %
(0; 20)	0.4552	0.5291	0.4531
(20; 40)	0.3347	0.3762	0.3339
(40; 60)	0.2267	0.2910	0.2662
(60; 80)	0.2238	0.2410	0.2236
(80; 100)	0.2047	0.2058	0.2047

It should be noted that the result of measurements by the proposed method is an average viscosity estimate, since the calculation algorithm

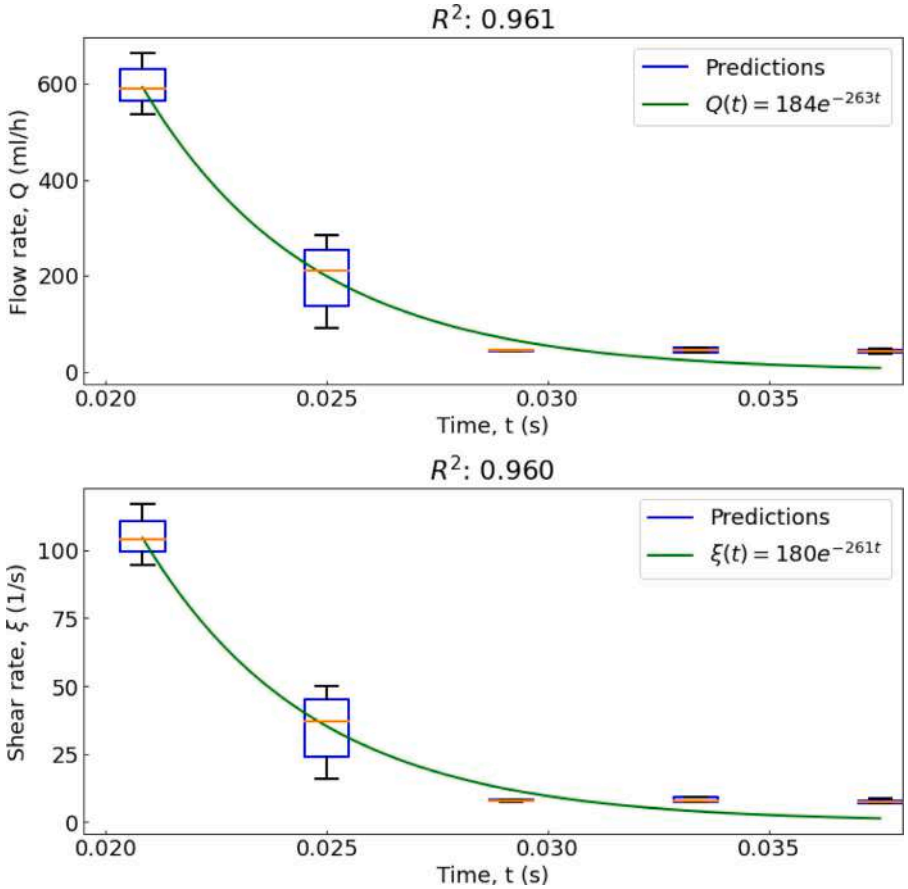

Fig. 13. The flow rate and the shear rate values predicted by the convolutional neural network inference model CNN_2. The predictions are presented in the form of box plots and the green curves show the averaged predictions of the model for 10 parallel physical tests. (see Section 5.2).

is based on the fitting model based on the deep neural network. However, for a new test under the same conditions (same fluid, same temperature, etc.), the network predictions will differ slightly from the previous one, because the images of the fluid flow obtained during the test are fed to the input.

During the study, the following results were obtained:

- the conditions that ensure the homogeneity of the thermal and mechanical quantities distribution and recommendations on sizes and operating modes of the novel inertial viscometer were formulated on the basis of the analysis of the dimensionless mathematical model of the inertial fluid flow in a toroidal channel;

- analysis of the fluid flow simulation model allowed to determine that the duration of the inertial fluid flow does not depend on the initial torus speed but it depends on the kind of fluid. Therefore, the choice of the initial rotation speed is connected with the range of shear rates under study. It is shown that at the initial rotation frequency n=50 rpm, the shear rates range is 0–200 s^{-1}. In general, the flow duration is less than 1 s. All the theoretical conclusions were confirmed during the experiments with the test setup;

- it was found that the values of the spatial speckle contrast calculated using a sequence of images make it possible to predict the kinematic characteristics of the flow, such as the flow rate through the capillary of the torus and the shear rate on the inner surface of the torus;

- the proposed inference CNN model based on the ResNet18 architecture that receives the LSCI data obtained from CMOS camera predicts the flow rate and shear rate with high accuracy;

- a novel viscosity measurement method for non-Newtonian fluids based on a combination of the numerical solution of the simplified Navier–Stokes equation and application of an artificial intelligence model for the computer vision system equipped with CMOS camera and laser illumination has been developed.

The advantages of the method include the ability to obtain a set of viscosity values in a given shear rates range in just one test; the duration of one measurement is less than 1 s; a small volume of the test fluid is required (1.87 ml); the homogeneity of the temperature and pressure distributions are ensured.

The disadvantages of the method include the requirement for the type of the test fluid, namely, it must have the ability to reflect light, i.e. be a suspension with small particles (oils with various modifying additives, fat emulsions, as well as physiological fluids); the viscometer has rotating parts and complicated measuring system.

It is worth noting that, as with any machine learning method, training data is required. On the one hand, this is a disadvantage, because for new fluids, the predictive model may turn out to be ineffective, but on the other hand, it is possible to expand the training set and retrain the model according to the transfer learning principle. Therefore, further research should be aimed at expanding the classes of tested fluids and improving the accuracy of the method.

6. Conclusions and further prospects

Theoretical basics of viscosity measurement methods are based on knowledge of the strain-stress state in the fluid flow domain. In this work we argued theoretically and proved experimentally that the proposed torus shaped flow domain of the inertial viscometer provides uniform distributions for the shear rates on the torus surface, as well as the pressure and temperature throughout the torus capillary. As the result, the number of assumptions is minimized and the proposed method allows the viscosity measurement of non-Newtonian fluids with viscous

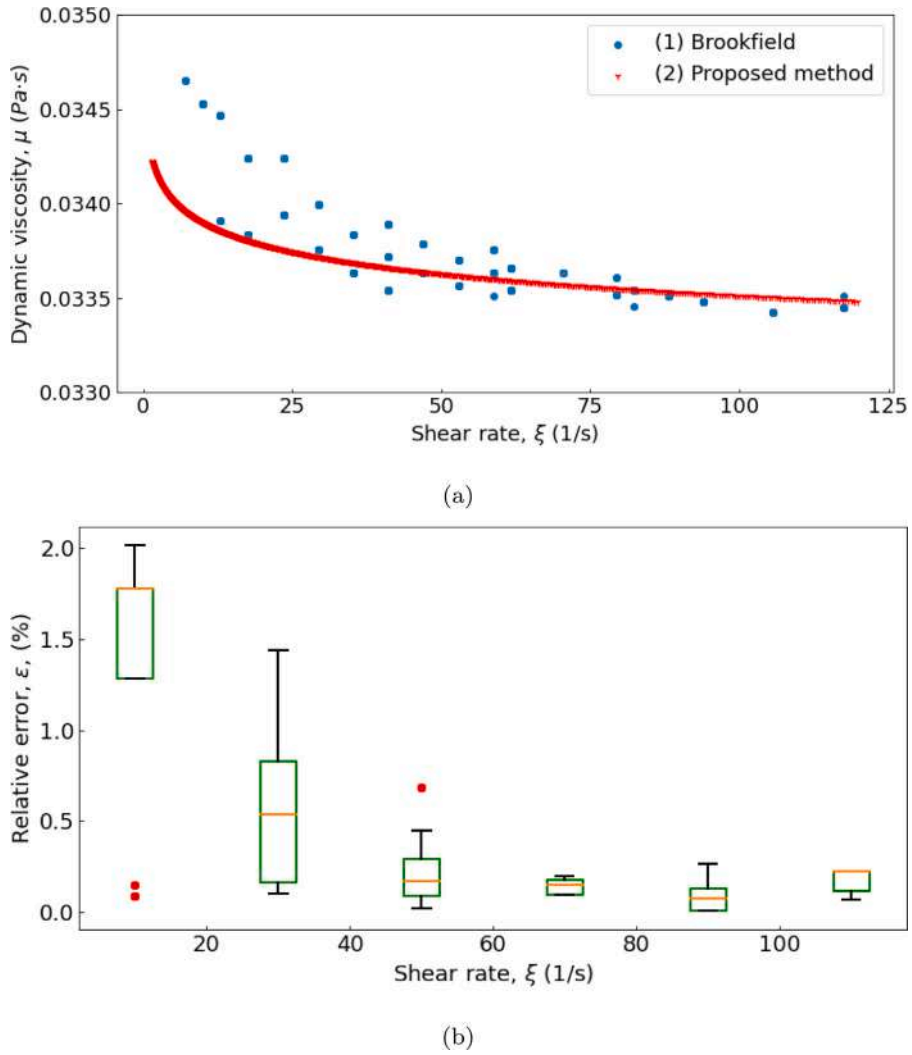

Fig. 14. Comparison of viscosity measurements of the test non-Newtonian fluid: (a) blue dot markers (1) represent the viscosity of the test fluid obtained using the Brookfield viscometer; red triangular markers (2) represent the viscosity values of the test fluid obtained using the proposed method; (b) the relative measurement errors obtained for each range of shear rates by both methods.

or viscoplastic properties. The challenging problem of measurements inside the torus is solved by means of application of the computer vision system and the speckle contrast imaging. The system operates with natural suspensions or fluids with ultrafine additives of relatively low viscosity (e.g. blood, urine, synovial fluid, water, glycerol, oils, etc.). The obtained results demonstrate that the relative error of the proposed method is less than 2% for the tested non-Newtonian fluid and less than 0.5% for the tested Newtonian fluid. Future research should be aimed at expanding the classes of tested fluids and the functionality of the computer vision system for extraction of some additional information on the state of the tested fluids.

CRediT authorship contribution statement

Elena P. Kornaeva: Supervision of the research, Methodology, Mathematical and simulation models in Sections 3, 5, Writing of the paper. **Ivan N. Stebakov:** Test setup modification and software engineering, Computer vision system software engineering, Data collection, Experiments, Validation of the experimental results, Graphics of the paper. **Alexey V. Kornaev:** Conceptualization of the inertial viscometer, Editing of the paper. **Viktor V. Dremin:** Computer vision system hardware engineering, Laser speckle contrast imaging, Editing of the paper. **Sergey G. Popov:** Test setup design and assembly. **Andrey Yu. Vinokurov:** Test fluid samples preparation, Validation of the viscosity measurement results.

Declaration of competing interest

The authors declare the following financial interests/personal relationships which may be considered as potential competing interests: Elena Kornaeva reports financial support was provided by Russian Science Foundation.

Data availability

Data will be made available on request.

Acknowledgments

This work was supported by the Russian Science Foundation under Project No. 20-79-00332. The authors gratefully acknowledge this support. The authors also express gratitude to Research and Development Center of Biomedical Photonics at Orel State University for the help with the experiments and for the opportunity to discuss the results of the research, and to Vera Panyushkina for the assistance with the translation of this paper.

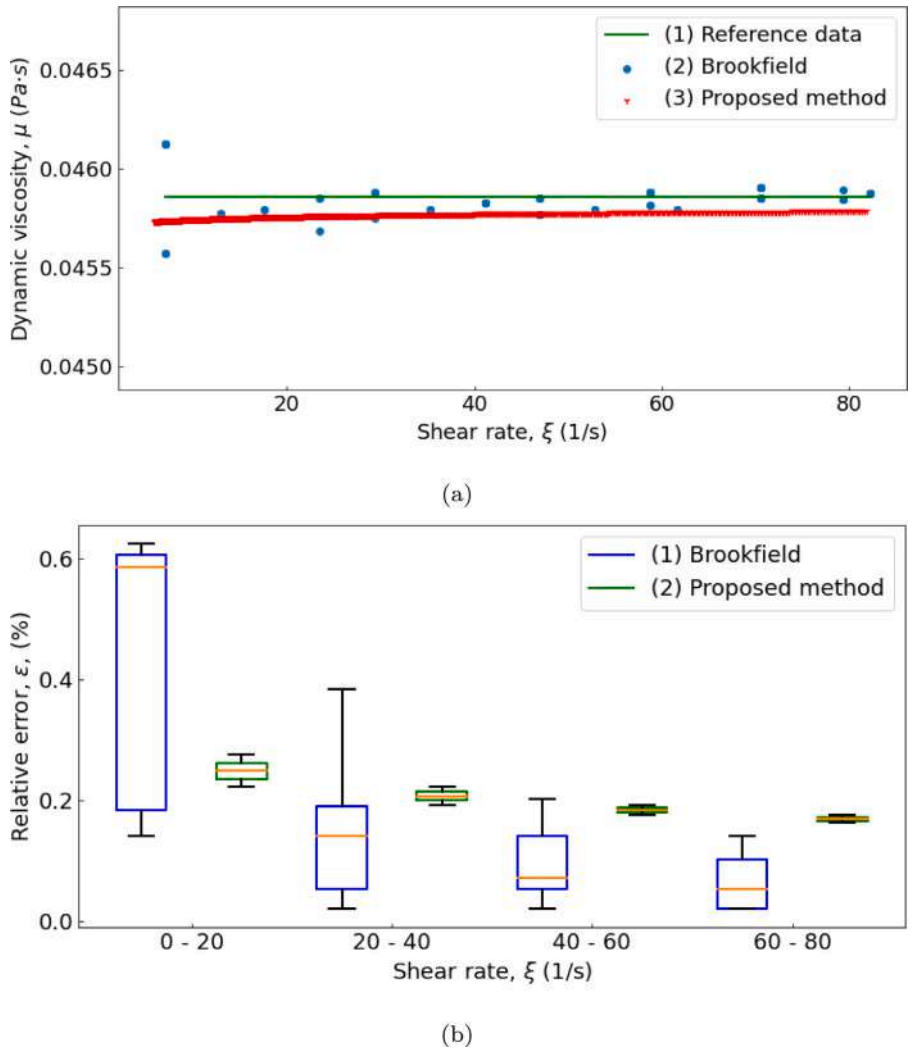

Fig. 15. Comparison of viscosity measurements of the test Newtonian fluid: (a) green continuous straight line (1) shows the reference value for the viscosity of the test fluid, taken from reference data in open sources; blue dot markers (2) represent the viscosity of the test fluid obtained using the Brookfield viscometer; red triangular markers (3) represent the viscosity values of the test fluid obtained using the proposed method. Zinc oxide suspension (0.1%) in 80% aqueous glycerol solution is considered as the test Newtonian solution. The viscosity value of the suspension corresponds to the reference value of the viscosity of 80% aqueous glycerol solution; (b) the relative measurement errors obtained for each range of shear rates by both methods.

Appendix A. Equations of the mathematical model

A.1. Derivation of the mathematical model equations

This section deals with Eqs. (1)–(4). The equations of a fluid flow in a toroidal channel are presented in a toroidal coordinate system β_i (see Fig. 1), which allows us to simplify these equations, as well as the boundary conditions.

The main model assumptions are presented below:

- the velocity field has only one nonzero component $\mathbf{V} = [[0\ v_2\ 0]]$ in toroidal coordinate system;

- due to the symmetry of the flow domain, the pressure is a function of two coordinates $p = p(\beta_1, \beta_3)$.

Under the condition of medium incompressibility $\rho = const$ the continuity equation [78] in curvilinear coordinates β_i has the form:

$$\frac{1}{H_1 H_2 H_3}\left(\frac{\partial(v_1 H_2 H_3)}{\partial \beta_1} + \frac{\partial(v_2 H_3 H_1)}{\partial \beta_2} + \frac{\partial(v_3 H_1 H_2)}{\partial \beta_3}\right) = 0, \tag{A.1}$$

where the Lame's coefficients for the toroidal coordinate system β_i have the form [79]:

$$H_1 = 1, H_2 = \beta_1 \cos\beta_3 + R, H_3 = \beta_1. \tag{A.2}$$

Then for the given velocity field $\mathbf{V} = [[0\ v_2\ 0]]$ the continuity equation (A.1) in the toroidal system β_i (A.2) takes the trivial form:

$$\frac{\partial}{\partial \beta_2}\left(H_3 v_2\right) = 0. \tag{A.3}$$

According to (A.3) the axial velocity depends on two coordinates: $v_2 = v_2(\beta_1, \beta_3)$.

The fluid motion equations are the Navier–Stokes equations [78] in curvilinear coordinates β_i for an incompressible fluid ($\rho = const$) have the general form[1]:

$$\rho\left(\frac{\partial v_i}{\partial t}+\frac{v_k}{H_k}\frac{\partial v_i}{\partial \beta_k}-\frac{v_k^2}{H_iH_k}\frac{\partial H_k}{\partial \beta_i}+\frac{v_kv_i}{H_kH_i}\frac{\partial H_i}{\partial \beta_k}\right)=\rho f_i-\frac{1}{H_i}\frac{\partial p}{\partial \beta_i}+ \\ +\frac{1}{H_i}\left(\frac{1}{H_1H_2H_3}\frac{\partial}{\partial \beta_j}\left(\frac{H_1H_2H_3H_i}{H_j}s_{ij}\right)-s_{mm}\frac{\partial \ln H_m}{\partial \beta_i}\right), \tag{A.4}$$

where ρ is a density of fluid; H_i are Lame's coefficients [79]; v_i are velocity components; ρf_i are body forces which are neglected for the considered flow; p is a pressure; s_{ij} are stress tensor components.

Stress tensor components s_{ij} can be expressed from the generalized Newtonian hypothesis [14,21] taking into account the incompressibility condition:

$$\mathbf{D}_\sigma = 2\mu\mathbf{D}_\xi,$$

where $\mathbf{D}_\sigma = [[s_{ij}]]$ and $\mathbf{D}_\xi = [[\xi_{ij}]]$ are strain stress and strain rate deviators.

According to the Stokes formula, the components of the strain rate tensor in curvilinear coordinates have the form:

$$\xi_{ik}=\frac{1}{2}\left(\frac{1}{H_k}\frac{\partial v_i}{\partial \beta_k}+\frac{1}{H_i}\frac{\partial v_k}{\partial \beta_i}-\frac{1}{H_iH_k}\left(v_i\frac{\partial H_i}{\partial \beta_k}+v_k\frac{\partial H_k}{\partial \beta_i}\right)+2\delta_{ik}\frac{v_m}{H_m}\frac{\partial \ln H_i}{\partial \beta_m}\right), \tag{A.5}$$

where δ_{ik} is the Kronecker delta.

According to the incompressibility condition, the deviator of the strain rate tensor is equal to the strain rate tensor $\mathbf{D}_\xi = \mathbf{T}_\xi$. Taking into account (A.3) the deviator of the strain rate tensor in toroidal coordinates (A.2) has the form:

$$\mathbf{D}_\xi=\left[\left[\begin{matrix}0 & \xi_{12} & 0\\ \xi_{21} & 0 & \xi_{23}\\ 0 & \xi_{32} & 0\end{matrix}\right]\right], \tag{A.6}$$

where $\xi_{12}=\xi_{21}=\frac{1}{2}\left(\frac{\partial v_2}{\partial \beta_1}-\frac{v_2}{H_2}\frac{\partial H_2}{\partial \beta_1}\right)$; $\xi_{23}=\xi_{32}=\frac{1}{2}\left(\frac{1}{H_3}\frac{\partial v_2}{\partial \beta_3}-\frac{v_2}{H_2H_3}\frac{\partial H_2}{\partial \beta_3}\right)$. Then, taking into account (A.3) and (A.6), the Navier–Stokes equations (A.4) have the form:

$$\frac{\partial p}{\partial \beta_1}=\rho\frac{1}{H_2}\frac{\partial H_2}{\partial \beta_1}v^2, \\ \rho\frac{\partial v}{\partial t}=\frac{1}{H_2^2H_3}\left(\frac{\partial}{\partial \beta_1}\left(H_2^2H_3s_{12}\right)+\frac{\partial}{\partial \beta_3}\left(H_2^2s_{23}\right)\right), \\ \frac{\partial p}{\partial \beta_3}=\rho\frac{1}{H_2}\frac{\partial H_2}{\partial \beta_3}v^2, \tag{A.7}$$

where $v_2 = v$ (hereinafter).

Under the condition of constancy of temperature properties in curvilinear coordinates β_i the equation of convective heat conduction [78] has the form:

$$\rho C_p\left(\frac{\partial T}{\partial t}+\frac{v_m}{H_m}\frac{\partial T}{\beta_m}\right)=\frac{\lambda\in'_{ijk}}{H_iH_jH_k}\frac{\partial}{\partial \beta_i}\left(\frac{H_jH_k}{H_i}\frac{\partial T}{\partial \beta_i}\right)+2\mu\xi_{pq}\xi_{pq}, \tag{A.8}$$

where C_p is the specific heat capacity; T is the temperature function; λ is the thermal conductivity; μ is the dynamic viscosity; ξ_{pq} are components of a strain rate tensor; $\in'_{ijk}$ is the Levi-Civita symbol only for an even permutation of $(1, 2, 3)$.

Taking into account (A.3) and (A.6), the equation of convective heat conduction (A.8) in toroidal coordinates has the form:

$$\rho C_p\frac{\partial T}{\partial t}=\frac{\lambda}{H_2H_3}\left(\frac{\partial}{\partial \beta_1}\left(H_2H_3\frac{\partial T}{\partial \beta_1}\right)+\frac{\partial}{\partial \beta_3}\left(\frac{H_2}{H_3}\frac{\partial T}{\partial \beta_3}\right)\right)+2\mu\left(\xi_{12}^2+\xi_{23}^2\right). \tag{A.9}$$

A.2. Dimensionless form of the mathematical model equations

The method of non-dimensionalization is presented in Table A.5. Dimensionless equations can be obtained by substitution of dimensional quantities expressed through dimensionless quantities. For example, according to Table A.5, the dimensional coordinate β_1 has the form $\beta_1 = r\widetilde{\beta}_1$ or the dimensional temperature function has the form $T = \Delta T\widetilde{T} + T_0$, and etc.

Table A.5
Dimensionless quantities.

Dimensionless quantity	$\widetilde{\beta}_1$	$\widetilde{\beta}_2$	$\widetilde{\beta}_3$	$\widetilde{H}_2$	$\widetilde{v}$	$\widetilde{p}$	$\widetilde{t}$	$\widetilde{T}$
Non-dimensional form	$\frac{\beta_1}{r}$	$\frac{\beta_1}{2\pi}$	$\frac{\beta_1}{2\pi}$	$\frac{H_2-(R-r)}{2r}$	$\frac{v}{V_0}$	$\frac{p}{p_0}$	$\frac{t}{t_0}$	$\frac{T-T_0}{\Delta T}$

Table A.6
Dimensionless terms of Eq. (A.14).

Inertial term	Dissipative terms									
$\frac{\partial \widetilde{v}}{\partial \widetilde{t}}$	$\frac{\partial^2 \widetilde{v}}{\partial \widetilde{\beta}_1^2}$	$\frac{\partial \widetilde{v}}{\partial \widetilde{\beta}_1}$		$\frac{\partial^2 \widetilde{v}}{\partial \widetilde{\beta}_3^2}$	$\frac{\partial \widetilde{v}}{\partial \widetilde{\beta}_3}$		$\widetilde{v}$			
$ReSh$	10^0	γ^{-1}	10^0	ψ^2	$\psi^2\gamma^{-1}$	ψ^2	γ^{-2}	γ^{-1}	$\psi^2\gamma^{-2}$	$\psi^2\gamma^{-1}$

Then, the Navier–Stokes equations (A.7) and the equation of convective heat conduction (A.9) can be presented as follows:

$$\widetilde{Eu}\frac{\partial \widetilde{p}}{\partial \widetilde{\beta}_1}=\frac{1}{\widetilde{H}_2+\gamma}\frac{\partial \widetilde{H}_2}{\partial \widetilde{\beta}_1}\widetilde{v}^2, \tag{A.10}$$

$$ShRe\frac{\partial \widetilde{v}}{\partial \widetilde{t}}=\frac{1}{\widetilde{H}_3(\widetilde{H}_2+\gamma)^2}\left(\frac{\partial}{\partial \widetilde{\beta}_1}\left(\widetilde{H}_3(\widetilde{H}_2+\gamma)^2\widetilde{s}_{12}\right)+\psi\frac{\partial}{\partial \widetilde{\beta}_3}\left((\widetilde{H}_2+\gamma)^2\widetilde{s}_{23}\right)\right), \tag{A.11}$$

$$\widetilde{Eu}\frac{\partial \widetilde{p}}{\partial \widetilde{\beta}_3}=\frac{1}{\widetilde{H}_2+\gamma}\frac{\partial \widetilde{H}_2}{\partial \widetilde{\beta}_3}\widetilde{v}^2, \tag{A.12}$$

$$ShRe\frac{\partial \widetilde{T}}{\partial \widetilde{t}}=\frac{1}{Pr}\frac{1}{\widetilde{H}_3(\widetilde{H}_2+\gamma)}\left(\frac{\partial}{\partial \widetilde{\beta}_1}\left(\widetilde{H}_3(\widetilde{H}_2+\gamma)\frac{\partial \widetilde{T}}{\partial \widetilde{\beta}_1}\right)+\psi^2\frac{\partial}{\partial \widetilde{\beta}_3}\left(\frac{\widetilde{H}_2+\gamma}{\widetilde{H}_3}\frac{\partial \widetilde{T}}{\partial \widetilde{\beta}_3}\right)\right)+ \\ +2Ec\widetilde{\mu}\left(\widetilde{\xi}_{12}^2+\widetilde{\xi}_{23}^2\right), \tag{A.13}$$

where $\widetilde{Eu} = p_0/(\rho V_0^2)$ is the Euler number analogue (hereinafter the Euler number); $Sh = r/(t_0V_0)$ is the Strouhal's number; $Re = V_0r/\eta_0$ is the Reynolds number; $Pr = \mu_0C_p/\lambda$ is the Prandtl number; $Ec = V_0^2/(C_p\Delta T)$ is the Eckert number; $\gamma = (R - r)/(2r)$, $\psi = 1/(2\pi)$ are the dimensionless geometric parameters; $\widetilde{\xi}_{12} = \widetilde{\xi}_{21} = \frac{1}{2}\left(\frac{\partial \widetilde{v}}{\partial \widetilde{\beta}_1}-\frac{\widetilde{v}}{\widetilde{H}_2+\gamma}\frac{\partial \widetilde{H}_2}{\partial \widetilde{\beta}_1}\right)$, $\widetilde{\xi}_{23}=\widetilde{\xi}_{32}=\frac{\psi}{2\widetilde{H}_3}\left(\frac{\partial \widetilde{v}}{\partial \widetilde{\beta}_3}-\frac{\widetilde{v}}{\widetilde{H}_2+\gamma}\frac{\partial \widetilde{H}_2}{\partial \widetilde{\beta}_3}\right)$ are the dimensionless strain rate tensor components; $\widetilde{s_{ij}} = 2\widetilde{\mu}\widetilde{\xi}$ are the stress tensor components; $V_0 = \omega R$ is the characteristic velocity; t_0 is the characteristic time of inertial fluid flow to stop; ΔT is the temperature change of the fluid; η_0 is the characteristic kinematic viscosity; ρ is the characteristic density.

Eq. (A.11) can be written in detail:

$$ShRe\frac{\partial \widetilde{v}}{\partial \widetilde{t}}=\widetilde{\mu}\frac{\partial^2 \widetilde{v}}{\partial \widetilde{\beta}_1^2}+\left(\frac{\widetilde{\mu}}{\widetilde{H}_2+\gamma}\frac{\partial \widetilde{H}_2}{\partial \widetilde{\beta}_1}+\frac{\widetilde{\mu}}{\widetilde{H}_3}\frac{\partial \widetilde{H}_3}{\partial \widetilde{\beta}_1}+\frac{\partial \widetilde{\mu}}{\partial \widetilde{\beta}_1}\right)\frac{\partial \widetilde{v}}{\partial \widetilde{\beta}_1}+\widetilde{\mu}\frac{\psi^2}{\widetilde{H}_3^2}\frac{\partial^2 \widetilde{v}}{\partial \widetilde{\beta}_3^2}+ \\ +\frac{\psi^2}{\widetilde{H}_3^2}\left(\frac{\widetilde{\mu}}{\widetilde{H}_2+\gamma}\frac{\partial \widetilde{H}_2}{\partial \widetilde{\beta}_3}+\frac{\partial \widetilde{\mu}}{\partial \widetilde{\beta}_3}\right)\frac{\partial \widetilde{v}}{\partial \widetilde{\beta}_3}-\frac{1}{\widetilde{H}_2+\gamma}\left(\frac{\widetilde{\mu}}{\widetilde{H}_2+\gamma}\left(\frac{\partial \widetilde{H}_2}{\partial \widetilde{\beta}_1}\right)^2+\right. \\ +\widetilde{\mu}\frac{\partial^2 \widetilde{H}_2}{\partial \widetilde{\beta}_1^2}+\frac{\widetilde{\mu}}{\widetilde{H}_3}\frac{\partial \widetilde{H}_2}{\partial \widetilde{\beta}_1}\frac{\partial \widetilde{H}_3}{\partial \widetilde{\beta}_1}+\frac{\partial \widetilde{H}_2}{\partial \widetilde{\beta}_1}\frac{\partial \widetilde{\mu}}{\partial \widetilde{\beta}_1}+\frac{\psi^2}{\widetilde{H}_3^2}\left(\frac{\widetilde{\mu}}{\widetilde{H}_2+\gamma}\left(\frac{\partial \widetilde{H}_2}{\partial \widetilde{\beta}_3}\right)^2+\right. \\ \left.\left.+\widetilde{\mu}\frac{\partial^2 \widetilde{H}_2}{\partial \widetilde{\beta}_3^2}+\frac{\partial \widetilde{H}_2}{\partial \widetilde{\beta}_3}\frac{\partial \widetilde{\mu}}{\partial \widetilde{\beta}_3}\right)\right)\widetilde{v}. \tag{A.14}$$

Table A.6 shows the dimensionless terms orders of Eq. (A.14). The dimensions of the channel are designed in such a way that the curvature of the channel can be neglected. Namely, the geometric parameter is taken as $\gamma \gg 0.5$ (see Section 3.1). The term with the coefficient $ReSh$

[1] Here and below, we use the Einstein notation.

on the left side of the equation has the highest order. With respect to this term in Eq. (A.14), only two terms are significant (the first and third term on the right side, see Table A.6). Then Eq. (A.14) can be written in a simplified form:

$$ShRe\widetilde{\beta}_1 \frac{\partial \widetilde{v}}{\partial \widetilde{t}} = \frac{\partial}{\partial \widetilde{\beta}_1}(\widetilde{\mu}\widetilde{\beta}_1 \frac{\partial \widetilde{v}}{\partial \widetilde{\beta}_1}). \quad (A.15)$$

Appendix B. Nomenclature

Operators and symbols	
i, j, k	Dummy indexes
$\in'_{ijk}$	Levi-Civita symbol only for an even permutation of (1, 2, 3)
δ_{ij}	Kronecker delta
$\mathbf{T}_\delta = [\![\delta_{ij}]\!]$	Unit tensor
$\nabla = [\![\frac{\partial}{\partial x_i}]\!]$	Hamiltonian
$\nabla\phi = [\![\frac{\partial\phi}{\partial x_i}]\!]$	Gradient of a scalar function
$\nabla \cdot \mathbf{y} = \frac{\partial y_i}{\partial x_i}$	Divergence
$\nabla \otimes \mathbf{y} = [\![\frac{\partial y_j}{\partial x_i}]\!]$, $\mathbf{y} \otimes \nabla = [\![\frac{\partial y_i}{\partial x_j}]\!]$	Gradients of a vector function
$\nabla \cdot \mathbf{T}_y = [\![\frac{\partial y_{ij}}{\partial x_j}]\!]$	Divergence of a tensor
$\mathbf{\Delta} = \frac{\partial^2}{\partial x_i \partial x_i}$	Laplacian
$\widetilde{y}$, y^*	Dimensionless and characteristic value, respectively
Geometry parameters	
β_i	Toroidal coordinate system
$H_1 = 1,\ H_2 = \beta_1 \cos\beta_3 + R,$ $H_3 = \beta_1$	Lamé's coefficients for a toroidal coordinates
L	Length (m)
r, R	Radius (m)
$\gamma = (R - r)/(2r)$, $\psi = 1/(2\pi)$	Dimensionless geometric parameters
x_i	Cartesian coordinates (m)
Kinematic parameters	
$\mathbf{T}_\xi = [\![\xi_{ij}]\!]$	Strain rate tensor (1/s)
$D_\xi = [\![\xi_{ij}]\!]$	Deviator part of the strain rate tensor (1/s)
ξ_0	Mean strain rate (1/s)
$\mathbf{V}$	Velocity vector, (m/s)
ω	Angular velocity (1/s)
$V_0 = \omega R$	Characteristic velocity
Q	Flow rate of fluid (m^3/s)
n	Torus rotation frequency (rpm)
η	kinematic viscosity of fluid (m^2/c)
Static parameters	
p	Fluid flow pressure or negative mean stress (Pa)
$T_\sigma = [\![\sigma_{ij}]\!]$	Stress tensor (Pa)
$D_\sigma = [\![s_{ij}]\!]$	Deviator part of the stress tensor (Pa)
Dynamic parameters	
μ, μ_0	Dynamic viscosity coefficient (viscosity) and mean viscosity, respectively (Pa s)
θ_0, θ_1	Parameters of the Ostwald model ($\mu(\xi) = \theta_0 \xi^{\theta_1 - 1}$), $\theta_1 < 1$ for pseudoplastic fluid
t	Time (s)
t_0	Characteristic time of inertial fluid flow to stop
ΔT	Temperature change of the fluid
C_p	Specific heat (J/(kg K))
λ	Thermal conductivity (W/(m K))
Dimensionless similarity criteria	
$\widetilde{Eu} = p_0/(\rho V_0^2)$	Analogue of the Euler number
$Sh = r/(t_0 V_0)$	Strouhal's number
$Re = V_0 r/\eta_0$	Reynolds number
$Pr = \mu_0 C_p/\lambda$	Prandtl number
$Ec = V_0^2/(C_p \Delta T)$	Eckert number
Laser speckle contrast parameters	
σ_n	Intensity standard deviation in subdomain
$\langle I_n \rangle$	mean intensity in subdomain
$K = \frac{\sigma_n}{\langle I_n \rangle}$	Spatial speckle-contrast
Metrics	
$MSE = \frac{1}{2n}\sum_{k=1}^{2}\sum_{i=1}^{n}\left(y_{true\,i}^{(k)} - y_{pred\,i}^{(k)}\right)^2$	Mean square error
$R^2 = 1 - \frac{\sum_{i=1}^{n}\left(y_{true\,i} - y_{pred\,i}\right)^2}{\sum_{i=1}^{n}\left(y_{true\,i} - \overline{y_{true}}\right)^2}$	Coefficient of determination
$RSD = \frac{\sqrt{\frac{1}{n}\sum_{i=1}^{n}\left(y_{true\,i} - y_{pred\,i}\right)^2}}{\overline{y_{true}}}$	Relative standard deviation
$\overline{\varepsilon} = \frac{\frac{1}{n}\sum_{i=1}^{n}\left\lvert y_{true\,i} - y_{pred\,i}\right\rvert}{\overline{y_{true}}}$	Mean relative error

References

[1] Harris M, Wirtz D, Wu P. Dissecting cellular mechanics: Implications for aging, cancer, and immunity. Sem Cell Dev Biol 2019;93:16–25.
[2] Yeow N, Tabor R, Garnier G. Atomic force microscopy: From red blood cells to immunohaematology. Adv Colloid Interface Sci 2017;249:149–62.
[3] Gertz M. Acute hyperviscosity: syndromes and management. Blood 2018;132:1379–85.
[4] Nader E, Skinner S, Romana M, Fort R, Lemonne N, Guillot N, et al. Blood rheology: Key parameters, impact on blood flow, role in sickle cell disease and effects of exercise. Front Physiol 2019;10:1329.
[5] Baskurt OK, Meiselman HJ. Blood rheology and hemodynamics. Semin Thromb Hemost 2003;29:435–50.
[6] Connes P, Alexy T, Detterich J, Romana M, Hardy-Dessources M, Ballas S. The role of blood rheology in sickle cell disease. Blood Rev 2016;30:111–8.
[7] Sochi T. Non-Newtonian rheology in blood circulation. 2013, p. 1–26, URL http://arxiv.org/abs/1306.2067.
[8] Chen J, Lu XY, Wang W. Non-Newtonian effects of blood flow on hemodynamics in distal vascular graft anastomoses. J Biomech 2006;39:1983–95.
[9] Mandal PK. An unsteady analysis of non-Newtonian blood flow through tapered arteries with a stenosis. Int J Non-Linear Mech 2005;40:151–64.
[10] Bodnar T, Sequeira A, Prosi M. On the shear-thinning and viscoelastic effects of blood flow under various flow rates. Appl Math Comput 2011;217:5055–67.
[11] Connes P, Dufour S, Pichon A, Favret F. Blood rheology, blood flow, and human health. Nutr Enhanc Sports Perform 2019;359–69.
[12] Middleman S. Continuum and molecular rheology. Interscience Publishers; 1968.
[13] Baskurt OK, Boynard M, Cokelet GC, Connes P, Cooke BM, Forconi S, et al. New guidelines for hemorheological laboratory techniques. Clin Hemorheol Microcirc 2009;42:75–97.
[14] Sequeira A. Hemorheology: Non-Newtonian constitutive models for blood flow simulations. In: Non-Newtonian fluid mechanics and complex flows. Lecture notes in mathematics, vol. 2212, Springer Verlag; 2018, p. 1–44.
[15] Wilkinson MA. Non-Newtonian fluids. In: Fluid mechanics, mixing and heat transfer. Pergamon Press; 1960.
[16] Molla MM, Paul MC. LES of non-Newtonian physiological blood flow in a model of arterial stenosis. Med Eng Phys 2012;34:1079–87.
[17] Chhabra R, Richardson J. Non-Newtonian flow in the process industries : fundamentals and engineering applications. Butterworth-Heinemann; 1999, p. 436.
[18] Jung JM, Lee DH, Cho YI. Non-Newtonian standard viscosity fluids. Int Commun Heat Mass Transfer 2013;49:1–4.
[19] More solutions to sticky problems. A guide to getting more from your Brookfield Viscometer & Rheometer. 2017, www.brookfieldengineering.com/downloads/technical-documents/. [Accessed 28 April 2022].
[20] Viswanath D, Ghosh T, Prasad D, Dutt N, Rany K. Viscosity of liquids. Springer; 2007.
[21] Kochin N, Kibel' I, Roze N. In: Radok J, editor. Theoretical hydromechanics. New York: Interscience Publishers; 1964.
[22] Kornaeva E, Kornaev A, Savin L. Inertial method of viscosity measurement of the complex rheology medium. Procedia Eng 2016;150:626–34.

[23] Revellin R, Rousset F, Baud D, Bonjour J. Extension of Murray's law using a non-Newtonian model of blood flow. Theor Biol Medical Model 2009;6.
[24] Kovacs D, Totsimon K, Biro K, Kenyeres P, Juricskay I, Kesmarky G, et al. Viscometer validation studies for routine and experimental hemorheological measurements. Clin Hemorheol Microcirc 2018;69:383–92.
[25] Mustafa A, Eser A, Aksu AC, Kiraz A, Tanyeri M, Erten A, et al. A micropillar-based microfluidic viscometer for Newtonian and non-Newtonian fluids. Anal Chim Acta 2020;1135:107–15.
[26] Kim H, Cho YI, Lee DH, Park CM, Moon HW, Hur M, et al. Analytical performance evaluation of the scanning capillary tube viscometer for measurement of whole blood viscosity. Clin Biochem 2013;46:139–42.
[27] Kawatra S, Bakshi A. On-line measurement of viscosity and determination of flow types for mineral suspensions. Process 1996;47:275–83.
[28] Gautam S, Guria C. An accurate determination of the shear rate for high-yield-stress drilling fluids using concentric cylinder fann 35 viscometer data. SPE J 2020;25:2984–3001.
[29] Joye DD. Shear rate and viscosity corrections for a casson fluid in cylindrical (Couette) geometries. J Colloid Interface Sci 2003;267:204–10.
[30] Lee E, Kim B, Choi S. Hand-held, automatic capillary viscometer for analysis of Newtonian and non-Newtonian fluids. Sensors Actuators A 2020;313.
[31] Oh S, Choi S. 3D-printed capillary circuits for calibration-free viscosity measurement of Newtonian and non-Newtonian fluids. Micromachines 2018;9:314.
[32] Oh S, Kim B, Lee JK, Choi S. 3D-printed capillary circuits for rapid, low-cost, portable analysis of blood viscosity. Sensors Actuators B 2018;259:106–13.
[33] Shin S, Keum D-Y. Viscosity measurement of non-Newtonian fluid foods with a mass-detecting capillary viscometer. J Food Eng 2002;5–10.
[34] Ferraz RS, Mello TP, Filho MNB, Borges RF, Filho SCM, Scheid CM, et al. An experimental and theoretical approach on real-time control and monitoring of the apparent viscosity by fuzzy-based control. J Pet Sci Eng 2022;217.
[35] Hapanowicz J. Proposition of non-standard method useful for viscosity measurements of unstable two-phase systems coupled with examples of its application. Meas: J Int Meas Confed 2020;164.
[36] Calvignac B, Rodier E, Letourneau J, Vitoux P, Aymonier C, Fages J. Development of an improved falling ball viscometer for high-pressure measurements with supercritical CO_2. J Supercrit Fluids 2010;55:96–106.
[37] Cristescu ND, Conrad BP, Tran-Son-Tay R. A closed form solution for falling cylinder viscometers. Internat J Engrg Sci 2002;40:605–20.
[38] Rolling-ball viscometer: Lovis 2000 M/ME. 2022, www.anton-paar.com/uk-en/products/details/rolling-ball-viscometer-lovis-2000-mme/. [Accessed 28 April 2022].
[39] Yamamoto H, Yabuta T, Negi Y, Horikawa D, Kawamura K, Tamura E, et al. Measurement of human blood viscosity a using Falling Needle Rheometer and the correlation to the modified Herschel-Bulkley model equation. Heliyon 2020;6:e04792.
[40] Sato Y, Baba H, Yoneyama C, Inomata H. Development of a rolling ball viscometer for simultaneous measurement of viscosity, density, bubble-point pressure of CO_2-expanded liquids. Fluid Phase Equilib 2019;487:71–5.
[41] Hubbard RM, Granger G. The rolling ball viscometer. Ind Eng Chem Anal Ed 1943;15:212–8.
[42] Camas-Anzueto JL, Gómez-Pérez J, Meza-Gordillo R, Anzueto-Sánchez G, Pérez-Patricio M, López-Estrada FR, et al. Measurement of the viscosity of biodiesel by using an optical viscometer. Flow Meas Instrum 2017;54:82–7.
[43] Singh P, Sharma K, Puchades I, Agarwal PB. A comprehensive review on MEMS-based viscometers. Sensors Actuators A 2022;338:113456.
[44] Elizalde E, Urteaga R, Berli CLA. Precise capillary flow for paper-based viscometry. Microfluid Nanofluidics 2016;20:135.
[45] Puneeth SB, Goel S. Handheld and 'Turnkey' 3D printed paper-microfluidic viscometer with on-board microcontroller for smartphone based biosensing applications. Anal Chim Acta 2021;1153:338303.
[46] Bianco M, Zizzari A, Gazzera L, Metrangolo P, Gigli G, Viola I, et al. Integrated microfluidic viscometer for edible oil analysis. Sensors Actuators B 2018;265:91–7.
[47] Jang I, Berg KE, Henry CS. Viscosity measurements utilizing a fast-flow microfluidic paper-based device. Sensors Actuators B 2020;319.
[48] Srivastava N, Burns M. Analysis of non-Newtonian liquids using a microfluidic capillary viscometer. Anal Chem 2006;78:1690–6.
[49] Lan WJ, Li SW, Xu JH, Luo GS. Rapid measurement of fluid viscosity using co-flowing in a co-axial microfluidic device. Microfluid Nanofluidics 2010;8:687–93.
[50] Nguyen NT, Yap YF, Sumargo A. Microfluidic rheometer based on hydrodynamic focusing. Meas Sci Technol 2008;19:085405.
[51] Tzeng BB, Sun YS. Design and fabrication of a microfluidic viscometer based on electrofluidic circuits. Micromachines 2018;9:375.
[52] Khnouf R, Karasneh D, Abdulhay E, Abdelhay A, Sheng W, Fan Z. Microfluidics-based device for the measurement of blood viscosity and its modeling based on shear rate, temperature, and heparin concentration. Biomed Microdevices 2019;21.
[53] Goodman J. Speckle phenomena in optics: theory and applications. Robert and Company Publisher; 2007.
[54] Dremin V, Kozlov I, Volkov M, Margaryants N, Potemkin A, Zherebtsov E, et al. Dynamic evaluation of blood flow microcirculation by combined use of the laser Doppler flowmetry and high-speed videocapillaroscopy methods. J Biophotonics 2019;12.
[55] Mizeva I, Dremin V, Potapova E, Zherebtsov E, Kozlov I, Dunaev A. Wavelet analysis of the temporal dynamics of the laser speckle contrast in human skin. IEEE Trans Biomed Eng 2020;67(7):1882–9.
[56] McNamee AP, Fitzpatrick T, Tansley GD, Simmonds MJ. Sublethal supraphysiological shear stress alters erythrocyte dynamics in subsequent low-shear flows. Biophys J 2020;119:2179–89.
[57] Daly S, Leahy M. 'Go with the flow': A review of methods and advancements in blood flow imaging. J Biophotonics 2013;6:217–55.
[58] Draijer M, Hondebrink E, Leeuwen TV, Steenbergen W. Review of laser speckle contrast techniques for visualizing tissue perfusion. Lasers Med Sci 2009;24:639–51.
[59] Stebakov I, Kornaeva E, Stavtsev D, Potapova E, Dremin V. Laser speckle contrast imaging and machine learning in application to physiological fluids flow rate recognition. Vibroeng Procedia 2021;38:50–5.
[60] Potapova E, Seryogina E, Dremin V, Stavtsev D, Kozlov I, Zherebtsov E, et al. Laser speckle contrast imaging of blood microcirculation in pancreatic tissues during laparoscopic interventions. Quantum Electron 2020;50(1):33–40.
[61] The AI index report – artificial intelligence index. 2022, URL https://aiindex.stanford.edu/report/.
[62] Goodfellow I, Bengio Y, Courville A. Deep learning. MIT Press; 2016, http://www.deeplearningbook.org.
[63] Zerka F, Urovi V, Bottari F, Leijenaar RT, Walsh S, Gabrani-Juma H, et al. Privacy preserving distributed learning classifiers – Sequential learning with small sets of data. Comput Biol Med 2021;136:104716.
[64] Izonin I, Tkachenko R. Universal intraensemble method using nonlinear AI techniques for regression modeling of small medical data sets. In: Bhoi AK, de Albuquerque VHC, Srinivasu PN, Marques G, editors. Cognitive and soft computing techniques for the analysis of healthcare data. Academic Press; 2022, p. 123–50.
[65] Brigato L, Iocchi L. A close look at deep learning with small data. Proc Int Conf Pattern Recognit 2020;2490–7, URL https://arxiv.org/abs/2003.12843v3.
[66] Moreno-Barea FJ, Jerez JM, Franco L. Improving classification accuracy using data augmentation on small data sets. Expert Syst Appl 2020;161:113696.
[67] Member JGS, Tassi CRN, Ali M, Lee J, Humt M, Feng J, et al. A survey of uncertainty in deep neural networks. 2021, URL https://arxiv.org/abs/2107.03342v3.
[68] Huang Y, Bai B, Zhao S, Bai K, Wang F. Uncertainty-aware learning against label noise on imbalanced datasets. Proc AAAI Conf Artif Intell 2022;36:6960–9, URL https://arxiv.org/abs/2207.05471v1.
[69] Ghanem R, Higdon D, Owhadi H. Introduction to uncertainty quantification. In: Handbook of uncertainty quantification. Springer International Publishing; 2017, p. 3–6.
[70] Irvin J, Rajpurkar P, Ko M, Yu Y, Ciurea-Ilcus S, Chute C, et al. CheXpert: A large chest radiograph dataset with uncertainty labels and expert comparison. Proc Innov Appl Artif Intell Conf 2019.
[71] Rajpurkar P, Irvin J, Zhu K, Yang B, Mehta H, Duan T, et al. CheXNet: Radiologist-level pneumonia detection on chest X-Rays with deep learning. 2017, URL http://arxiv.org/abs/1711.05225.
[72] Lensink K, Lo FJ, Eddy RL, Law M, Laradji I, Haber E, et al. A soft labeling approach to develop automated algorithms that incorporate uncertainty in pulmonary opacification on chest CT using COVID-19 pneumonia. Academic Radiol 2022;29:994–1003.
[73] Lu L, Yin M, Fu L, Yang F. Uncertainty-aware pseudo-label and consistency for semi-supervised medical image segmentation. Biomed Signal Process Control 2023;79:104203.
[74] Malinin A, Gales M. Predictive uncertainty estimation via prior networks. In: Bengio S, Wallach H, Larochelle H, Grauman K, Cesa-Bianchi N, Garnett R, editors. Advances in neural information processing systems. vol. 31. Curran Associates, Inc.; 2018.
[75] Ashukha A, Lyzhov A, Molchanov D, Vetrov D. Pitfalls of in-domain uncertainty estimation and ensembling in deep learning. 2020, arXiv URL https://arxiv.org/abs/2002.06470.
[76] Rahaman R, thiery a. Uncertainty quantification and deep ensembles. In: Ranzato M, Beygelzimer A, Dauphin Y, Liang P, Vaughan JW, editors. Advances in neural information processing systems. vol. 34. Curran Associates, Inc.; 2021, p. 20063–75.
[77] Wójcik B, Grela J, Śmieja M, Misztal K, Tabor J. SLOVA: Uncertainty estimation using single label one-vs-all classifier. Appl Soft Comput 2022;126:109219.
[78] Patankar S. Numerical heat transfer and fluid flow. CRC Press; 2018.
[79] Korn G, Korn T. Mathematical handbook for scientists and engineers. Dover Publications; 2000.
[80] Tissue properties. 2022, www.itis.swiss/virtual-population/tissue-properties/database/database-summary/. [Accessed 28 April 2022].
[81] Kirkpatrick SJ, Duncan DD, Wells-Gray EM. Detrimental effects of speckle-pixel size matching in laser speckle contrast imaging. Opt Lett 2008;33(24):2886–8.
[82] Kingma D, Ba J. Adam: a method for stochastic optimization. In: 2015 ICLR conference. 2015.